

Estimation of bipolar jets from accretion discs around Kerr black holes

Rajiv Kumar¹, Indranil Chattopadhyay^{2*}

¹*Department of Astronomy, Xiamen University, Xiamen, Fujian 361005, China*

²*Aryabhata Research Institute of Observational Sciences (ARIES), Manora Peak, Nainital-263002, India*

ABSTRACT

We analyse flows around a rotating black hole and obtain self-consistent accretion-ejection solutions in full general relativistic prescription. Entire energy-angular momentum parameter space is investigated in the advective regime to obtain shocked and shock-free accretion solutions. Jet equations of motion are solved along the von-Zeipel surfaces computed from the post-shock disc, simultaneously with the equations of accretion disc along the equatorial plane. For a given spin parameter, the mass outflow rate increases as the shock moves closer to the black hole, but eventually decreases, maximizing at some intermediate value of shock location. Interestingly, we obtain all types of possible jet solutions, for example, steady shock solution with multiple critical points, bound solution with two critical points and smooth solution with single critical point. Multiple critical points may exist in jet solution for spin parameter $a_s \geq 0.5$. The jet terminal speed generally increases if the accretion shock forms closer to the horizon and is higher for corotating black hole than the counter-rotating and the non-rotating one. Quantitatively speaking, shocks in jet may form for spin parameter $a_s > 0.6$ and jet shocks range between $6r_g$ and $130r_g$ above the equatorial plane, while the jet terminal speed $v_{j\infty} > 0.35c$ if Bernoulli parameter $\mathcal{E} \geq 1.01$ for $a_s > 0.99$.

Key words: accretion, accretion discs - black hole physics - hydrodynamics - shock waves- galaxies: jets.

1 INTRODUCTION

Accretion powers many astrophysical objects, like active galactic nuclei (AGNs) and microquasars. Extreme luminosities of AGNs ($L \sim 10^{42-48}$ erg s⁻¹) and micro quasars ($L \sim 10^{36-39}$ erg s⁻¹) are thought to arise due to accretion

of matter and energy on to compact objects like black holes (BHs). AGNs are supposed to harbour supermassive BHs ($\sim 10^{6-9}M_\odot$, where M_\odot is the solar mass) and microquasars are supposed to harbour stellar mass BHs ($\sim 10M_\odot$). In addition, jets or transonic, relativistic, collimated outflows are quite common and are associated with most of these objects (Mirabel et. al. 1992; Mirabel & Rodriguez 1994; Ferrari

* E-mail: kumar@xmu.edu.cn (RK); indra@aries.res.in (IC)

1998; Junor *et al.* 1999; Doeleman *et al.* 2012). Since BHs do not have atmosphere so jets have to originate from the accreting matter. Although the exact mechanism by which these jets are launched is still a topic of active research, some salient properties of jets have been established from observations. Junor *et al.* (1999) observed that the jet from AGN M87 has to originate from a region $< 100r_s$ (r_s is the radius of non-rotating BH or Schwarzschild radius), while later interpretation of observational data reduced the estimate of the jet base even further (Doeleman *et al.* 2012). Such direct estimate of the jet base is yet to be obtained for microquasars. However, since the time-scales of microquasars and AGNs can be scaled by the central mass, so one can conclude that the basic physics of AGNs and microquasars are quite similar (McHardy *et al.* 2006). Moreover, similarities of jet-disc connection were observed in AGNs and microquasars (Marscher *et al.* 2002). This indicates that the jet base for microquasars should also be quite close to the central BH, as was observed for AGN.

Microquasars undergo a regular luminosity and spectral state changes within a time-scale of few months. There are two canonical spectral states: the low-hard state or LHS — low luminosity but radiative power maximizes in the high-energy power law part; and high-soft state or HSS — luminous and power maximizes in the low-energy thermal part of the spectra. It has been observed that many microquasars in outburst states make transition from LHS to HSS through a series of intermediate states, and this cycle repeats in some sort of hysteresis. In the hardness-intensity space this curve looks loosely like a ‘Q’ (Fender *et al.* 2004). The most interesting aspect of this property of microquasars is that the jet observed also varies with this cycle (Gallo *et al.* 2003). During HSS there is no jet, while weak quasi-steady jets start to form in LHS. As the microquasar moves to intermediate hard states, the jet strength increases (Rushton *et al.* 2010). And finally very strong jets are ejected while the microquasar makes a transition from hard intermediate to soft intermediate states. Eventually, the microquasar enters into HSS, which is luminous but jet is not detected. The important point these observations have established is that the jet states are deeply linked with the accretion states,

i. e., accretion discs are responsible for the jet generation. And by virtue of the similarity between AGNs and microquasars (McHardy *et al.* 2006), one can conclude that even for AGNs, the accretion disc is responsible for launching the jet.

It was understood quite early that the accreting matter needs to be rotating because radial accretion would be ‘too fast’ and would not have the time to generate such high luminosities. The first viable accretion disc model was proposed by Shakura & Sunyaev (1973), where the disc material possess Keplerian angular momentum, negligible advection and are optically thick, which quickly radiates the dissipated viscous energy into radiation. The extension to general relativity was done in the same year by Novikov & Thorne (1973). In spite of the obvious theoretical shortcomings such as the simplistic manner with which the inner edge of the disc or the pressure term was handled, even then, the Keplerian disc could still explain the thermal, modified blackbody part of the spectra. Therefore, one may conclude that the HSS is a state dominated by Keplerian disc. The power-law part of the spectra is not generated by Keplerian disc, and search for the component of the disc that generates the hard power-law tail in the spectra launched many competing accretion disc models. Among various disc models, thick disc (Paczynski & Wiita 1980) and advection-dominated accretion flows (Narayan & Yi 1994; Narayan *et al.* 1997) are notable. Both Keplerian disc and thick disc models are rotation dominated with negligible advection and therefore wholly subsonic. Advection-dominated accretion flows do not suffer from such limitations, but the boundary conditions were such that the solution is generally subsonic, and becomes transonic only close to the horizon. Simultaneous to this development, investigations in the advective regime showed some interesting aspects, like multiple sonic points (Liang & Thompson 1980), as well as existence of steady shocks (Fukue 1987; Chakrabarti 1989). Infact, Lu *et al.* (1999) showed that advection-dominated flows are indeed a subset of general advective accretion solutions. Moreover, it was clear from numerical simulations that post-shock disc (PSD), due to extra thermal energy gained by shock dissipation can deflect a fraction

of accreting matter along the rotation axis of the disc to produce precursor of jets (Molteni *et al.* 1994, 1996a,b; Lanzafame *et al.* 1998; Das *et al.* 2014; Lee *et al.* 2016). Semi-analytical versions of these studies have been extended into the dissipative regime for flows described by fixed Γ ($= c_p/c_v$ adiabatic index) equation of state (EoS; Becker *et al.* 2008; Kumar & Chattopadhyay 2013; Kumar *et al.* 2014; Aktar *et al.* 2015), as well as variable Γ EoS (Kumar *et al.* 2013; Kumar & Chattopadhyay 2014). Since shock in accretion is formed close to the central object ($r_{\text{sh}} \lesssim \text{few} \times 10 r_s$) and PSD is the base of the jet, therefore, shocked advective discs satisfy one observational criterion, i. e., the entire accretion discs do not generate jet, only the inner region forms jet.

Existence of the dominant power-law photons in the LHS and intermediate states necessitates existence of a Comptonizing corona in addition to the Keplerian component of the disc (Sunyaev & Titarchuk 1980). Most of the modern accretion disc models differ in the source and location of this corona. For advective shocked disc, the PSD is the Comptonizing corona. In a model solution Chakrabarti & Titarchuk (1995) considered a disc composed of Keplerian matter in the equatorial plane and sub-Keplerian matter flanking it from the top and bottom. The sub-Keplerian matter suffers shock, puffs in the form of a torus (PSD) and the extra heat evaporates the Keplerian disc. Various spectral states are easily explained using this hybrid disc model. If the Keplerian accretion rate increases, the resulting extra soft photons cool down the PSD giving rise to the HSS, and if the sub-Keplerian accretion rate is higher, it supplies hotter electrons that result in dominant inverse Comptonized power-law photons as in LHS. All intermediate combinations of the two accretion rates give rise to other intermediate states. This was later confirmed via numerical simulation (Giri & Chakrabarti 2013). Infact it was shown that the shock in an advective accretion disc shifts towards the BH if viscosity is increased, for a disc of same outer boundary condition (Kumar & Chattopadhyay 2013, 2014; Kumar *et al.* 2014). As the shock forms closer to the BH, it becomes stronger, producing faster jets. When radiative moments were computed from the disc and dumped

on to the thermally driven jet, Kumar *et al.* (2014) showed that as the advective accretion disc moves from LHS to intermediate states, the mildly relativistic jet becomes much stronger, as was reported in observations (Rushton *et al.* 2010).

Although the advective disc solutions contain features that automatically explain some of the broad observational features (compact corona, compact jet base, spectral state changes), still most of the works were done in the pseudo-Newtonian regime (Paczýński & Wiita 1980; Artemova *et al.* 1996; Mukhopadhyay 2003; Chakrabarti & Mondal 2006). Full general relativistic treatment were few and far between (Liang & Thompson 1980; Lu 1985; Fukue 1987; Chakrabarti 1996; Peitz & Appl 1997; Fukumura & Tsuruta 2004; Nagakura & Yamada 2008; Chattopadhyay & Chakrabarti 2011; Chattopadhyay & Kumar 2016). Moreover, although in some of these papers Kerr metric was used, the issue of jet generation was not addressed (with the exception of Chattopadhyay & Kumar 2016, but in Schwarzschild metric). The more favoured model for jet generation in the community is magnetically driven jets (Blandford & Payne 1982; Camezind 1986; Fendt & Greiner 2001). These relativistic magnetohydrodynamic solutions were not self-consistently generated from the accretion disc. There are also models that depend on the extraction of the rotational energy of the BH to power jets (Penrose 1969; Blandford & Znajek 1977). Incidentally, the role of BH spin in powering jets has been claimed to be confirmed (Narayan & McClintock 2012), as well as been refuted (Fender *et al.* 2010; Russel *et al.* 2013). In this paper, we would like to obtain accretion disc solutions that generate bipolar jets around Kerr BHs and investigate the role of spin in influencing the jet solution. These results will be valid if the flow is weakly magnetized or if the magnetic field of disc is stochastic in nature. Since theoretical investigation on jet generation from advective disc around Kerr BH is almost non-existent, therefore, it remains an unattempted question. It may be noted that Fukumura & Kazanas (2007) studied jet generation from advective disc around Kerr BH, but the generation mechanism used was particle

acceleration at the accretion shock. Commendable as the work may be, however, the authors concentrated their efforts only in estimating the mass-loss and the jet solution was not followed up to any reasonable distance from the disc: moreover, a fixed Γ EoS was also used and hence our approach is quite different. One must mention that efforts have been made in estimating mass-loss from advective disc recently with pseudo-Kerr potential (Aktar et al. 2015). However, since the jet geometry in pseudo-Newtonian potential regime depends weakly on the BH spin, therefore, one should check the issue of jet generation in full general relativity, to ascertain the role of spin in influencing jet solution.

In this paper, we study advective accretion flow around spinning BH. Although our aim is to study self-consistently launched jets, we present a separate study of only the accretion process, before presenting the simultaneous accretion-ejection solution. The jets originate from shocked advective discs. The jet geometry is computed from the von Zeipel surfaces (VZS; Abramowicz 1971; Chakrabarti 1985) that we employed previously for jets from accretion discs around Schwarzschild BH (Chattopadhyay & Kumar 2016). We study the effect of BH spin on the possibility of jet generation, as well as how the jet terminal speed is affected by the spin. One interesting thing we noticed from earlier accretion-ejection studies is that the steady, thermally driven jets obtained in pseudo-Newtonian regime are weak (Kumar & Chattopadhyay 2013; Kumar et al. 2013), but become stronger if they are powered by radiation (Kumar et al. 2014) or by shock oscillation (Lee et al. 2016). However, the thermally driven jet is itself stronger in the general relativistic domain compared to the Newtonian regime (Chattopadhyay & Kumar 2016). Therefore, we would like to investigate whether the jet strength increases with BH spin. The jet geometry around a spinning BH is decidedly non-spherical. Is it possible to find shocks in jets mediated by the non-spherical cross-section? Interestingly, for jets around Schwarzschild BH no such shock in jets were obtained (Chattopadhyay & Kumar 2016). There are some suggestions that the soft gamma-ray tails in X-ray binaries are due to the presence of shock-accelerated elec-

trons in the jet, where the shock is situated close to the BH (Laurent et al. 2011). If steady shocks in jet are found to occur close to the BH, then it may support the conclusions of Laurent et al. (2011). We would like to explore these questions in details. The novelty of this paper lies in the fact that this is probably the first effort to investigate all possible jet solutions, including those having multiple sonic points and shocks, where the jets are computed self-consistently from accretion discs. Moreover, the fluid in accretion-jet system is assumed to be fully ionized electron-proton fluid, described by a relativistic EoS.

In the next section, we present simplifying assumptions and the governing equations. In Section 3, we outline the solution procedure. In Section 4, we present the results, and in Section 5, we draw concluding remarks.

2 MODEL EQUATIONS AND ASSUMPTIONS

The estimated temperature of accreting matter is very high: therefore the disc-jet system is likely to be a fully ionized plasma. Additionally, we assume the accretion disc-jet system to be axisymmetric. The accretion disc is assumed to be in hydrostatic equilibrium in the vertical direction and its advection time-scale is assumed to be shorter than the viscous time-scales. Equations of motion of both the accretion disc and the jet are similar in form, i.e., the conservation of four-divergence of the respective energy-momentum tensors and the four-mass fluxes. However, the flow geometries of the jet and accretion disc are quite different, so the equations of motion of these two entities are presented separately.

We choose geometrical units $G = M_{\text{BH}} = c = 1$, where G , M_{BH} and c are universal gravitational constant, mass of the black hole and speed of the light. Therefore, units of length, speed, angular momentum, energy, time and mass are GM_{BH}/c^2 , c , GM_{BH}/c , $M_{\text{BH}}c^2$, GM_{BH}/c^3 and M_{BH} , respectively.

2.1 The fluid, its EoS and the background metric

The energy-momentum tensor of the fully ionized fluid under the present set of assumptions is given by

$$T^{\mu\nu} = (e + p)u^\mu u^\nu + pg^{\mu\nu}, \quad (1)$$

where e , p and u^μ are the local energy density, local gas pressure and four-velocities, respectively. Here, $g^{\mu\nu}$ are metric components and indices μ, ν are $(0, 1, 2, 3)$. The governing equations of the relativistic fluids are energy-momentum conservation and in absence of particle creation, mass-flux conservation given by

$$T_{;\nu}^{\mu\nu} = 0, \quad (\rho u^\nu)_{;\nu} = 0, \quad (2)$$

where ρ is the mass density of the flow. The i th component of the relativistic Euler equation is obtained by projecting $T_{;\nu}^{\mu\nu} = 0$, with the help of projection tensor $h_\mu^i = \delta_\mu^i + u_\mu u^i$, i. e. $h_\mu^i T_{;\nu}^{\mu\nu} = 0$, or,

$$[(e + p)u^\nu u_{;\nu}^i + (g^{i\nu} + u^i u^\nu)_{p,\nu}] = 0, \quad (3)$$

The energy balance equation or entropy equation or the first law of thermodynamics is $u_\mu T_{;\nu}^{\mu\nu} = 0$, or

$$\left[\left(\frac{e + p}{\rho} \right) \rho_{,\mu} - e_{,\mu} \right] = 0. \quad (4)$$

A rotating BH is characterized by mass M_{BH} and spin parameter $a_s (= J/M_{\text{BH}})$, where J is angular momentum of the BH, since in the present unit system $M_{\text{BH}} = 1$: therefore, the analysis presented in this paper is applicable from stellar mass to supermassive BHs. The disc-jet system is composed of test fluid that flows in the background metric of a spinning BH, and is described by Kerr metric and in terms of Boyer-Lindquist coordinates it is given by

$$ds^2 = g_{\mu\nu} dx^\mu dx^\nu = g_{tt} dt^2 + 2g_{t\phi} dt d\phi + g_{r\tau} dr^2 + g_{\theta\theta} d\theta^2 + g_{\phi\phi} d\phi^2. \quad (5)$$

Here, $x^\mu = (x^0, x^1, x^2, x^3) \equiv (t, r, \theta, \phi)$ and $g_{tt} = -(1 - 2r/\Sigma)$, $g_{t\phi} = -2a_s r \sin^2 \theta / \Sigma$, $g_{r\tau} = \Sigma / \Delta$, $g_{\phi\phi} = (A/\Sigma) \sin^2 \theta$, $g_{\theta\theta} = \Sigma$ are the metric components, where, a_s is the spin parameter. Here, $A = (r^2 + a_s^2)^2 - \Delta a_s^2 \sin^2 \theta$, $\Sigma = r^2 + a_s^2 \cos^2 \theta$ and $\Delta = r^2 - 2r + a_s^2$. In the unit system used, the four-velocity components satisfy $u_\mu u^\mu = -1$. It is clear that for $a_s = 0$, the Kerr metric reduces to the Schwarzschild metric. In the other extreme, $a_s \sim 1$ gives extreme Kerr BHs. If the flow and the spinning BH are in the same direction, then it is a prograde flow, i. e. $1 \geq a_s > 0$ and if they are opposite, then the flow is retrograde or $-1 \leq a_s < 0$.

The equations of motion (equation 2) are a set of five

independent equations but have six variables. The fluid follows a relativistic Maxwell-Boltzmann distribution, which when integrated in the momentum space produces an exact relation between e , p and ρ and is called the exact relativistic EoS of the flow (Chandrasekhar 1939; Synge 1957; Cox & Giuli 1968). Ryu *et al.* (2006); Chattopadhyay (2008) and Chattopadhyay & Ryu (2009) proposed an approximate EoS that is very accurate but much simpler compared to the exact EoS. The fluid contains electrons, protons and positrons of different proportions, such that the fluid is wholly neutral (total charge is zero) and the EoS is given by

$$e = n_e m_e c^2 f = \frac{\rho}{\tau} f, \quad (6)$$

where, $\rho (= \rho_e \tau = n_e m_e \tau)$ is the total mass density (see details in Chattopadhyay 2008; Chattopadhyay & Ryu 2009), $\tau = [2 - \xi(1 - 1/\chi)]$ and

$$f = (2 - \xi) \left[1 + \Theta \left(\frac{9\Theta + 3}{3\Theta + 2} \right) \right] + \xi \left[\frac{1}{\chi} + \Theta \left(\frac{9\Theta + 3/\chi}{3\Theta + 2/\chi} \right) \right]. \quad (7)$$

Here, $\xi = n_p/n_e$ is the composition parameter, $\Theta = (kT)/(m_e c^2)$ is the dimensionless temperature of the fluid and $\chi = m_e/m_p$ is the mass ratio, i. e. ratio between the electron mass and the proton mass. Here, n_p and n_e are the proton number density and the electron number density, respectively. The equivalence of the different forms of exact relativistic EoS (Chandrasekhar 1939; Synge 1957; Cox & Giuli 1968) and its comparison with the Chattopadhyay–Ryu approximate EoS show a very close agreement Vyas *et al.* (2015). In the relativistic case, polytropic index (N), the adiabatic index (Γ) and sound speed (a) are defined as,

$$N = \frac{1}{2} \frac{df}{d\Theta}; \quad \Gamma = 1 + \frac{1}{N} \quad \text{and} \quad a^2 = \frac{\Gamma p}{e + p} = \frac{2\Gamma\Theta}{f + 2\Theta}. \quad (8)$$

In this paper, we have investigated only the electron–proton case i.e., $e - p$ or $\xi = 1.0$. In the following, we present the equations of motion of the accretion disc and the jet separately.

2.2 Accretion Equations of motion

The accretion disc occupies the space around the equatorial plane of the BH. The equations of motion for the accretion disc are written on the equatorial plane (i.e., $\theta \rightarrow \pi/2$). The motion along the transverse direction is negligible i.e.,

$u^\theta = 0$. The flow variables are considered on the equatorial plane and assumed to remain constant along the transverse direction (i. e., $\partial/\partial\theta = 0$) while axisymmetry renders $\partial/\partial\phi = 0$.

The radial component of momentum balance equation (3), is

$$u^r \frac{du^r}{dr} + \frac{1}{2} g^{rr} g_{tt,r} g^{tt} + \frac{1}{2} u^r u^r [g^{tt} g_{tt,r} + g^{rr} g_{rr,r}] - \frac{1}{2} g^{rr} g_{tt,r} g^{t\phi} u^t u_\phi + \frac{1}{2} g^{rr} u^\phi u^\phi [g_{\phi\phi} g^{tt} g_{tt,r} - g_{\phi\phi,r}] + \frac{1}{2} g^{rr} u^t u^\phi [g_{t\phi} g^{tt} g_{tt,r} - 2g_{t\phi,r}] + \frac{(g^{rr} + u^r u^r)}{e+p} \frac{dp}{dr} = 0. \quad (9)$$

The integrated form of the azimuthal component ($h_\mu^\phi T_{;\nu}^{\mu\nu} = 0$) of energy-momentum conservation of equation (2) is

$$L = hu_\phi = \text{constant} = hl; \quad h = \frac{e+p}{\rho} = \frac{f+2\Theta}{\tau}, \quad (10)$$

where h is the specific enthalpy, L is the bulk angular momentum of the flow per unit mass, while the definition of specific angular momentum is $\lambda = -u_\phi/u_t$. The covariant ϕ component of the four-velocity is also represented as $l = u_\phi$. One may also obtain equation (10) with the aid of an azimuthal Killing vector $\zeta_\phi^\mu = (0, 0, 0, 1)$. The θ component of momentum balance equation (3) can be integrated assuming hydrostatic equilibrium around the equatorial plane (i.e. $\theta \approx \pi/2$) to obtain local disc half-height expression (Riffert & Herold 1995; Peitz & Appl 1997),

$$H = rH_\theta = \left(\frac{p r^3}{\rho \mathcal{F}} \right)^{1/2}, \quad (11)$$

where $\mathcal{F} = \gamma_\phi^2 [(r^2 + a_s^2)^2 + 2\Delta a_s^2] [(r^2 + a_s^2)^2 - 2\Delta a_s^2]^{-1}$. Integrating conservation of mass flux in equation (2), we obtain the expression of accretion rate,

$$\dot{M} = \int r^2 \rho u^r d\theta d\phi = 4\pi r^2 H_\theta \rho u^r = 4\pi \rho H u^r r. \quad (12)$$

If one integrates equation (4), we obtain the adiabatic EoS for relativistic multispecies adiabatic flow with the help of EoS (equation 6) as (Chattopadhyay & Kumar 2013, 2016; Kumar *et al.* 2013)

$$\rho = \mathcal{K} e^{k_3} \Theta^{3/2} (3\Theta + 2)^{k_1} (3\Theta + 2/\chi)^{k_2}, \quad (13)$$

where \mathcal{K} is the entropy constant and $k_1 = 3(2 - \xi)/4$, $k_2 = 3\xi/4$, $k_3 = (f - \tau)/(2\Theta)$. This relativistic equation is analogous to non-relativistic polytropic EoS, $p = \mathcal{K} \rho^\Gamma$. Using equation (13) in equation (12), we get entropy-accretion rate,

$$\dot{M} = \frac{\dot{M}}{4\pi \mathcal{K}} = u^r H r e^{k_3} \Theta^{3/2} (3\Theta + 2)^{k_1} (3\Theta + 2/\chi)^{k_2}, \quad (14)$$

\dot{M} is a constant for adiabatic flow.

Since $\partial g_{\mu\nu}/\partial t = 0$, so one may obtain a constant of motion with the help of a time-like Killing vector $\zeta_t^\mu = (1, 0, 0, 0)$ in the equation of motion we have

$$(\zeta_t^\mu T_\mu^\nu)_{;\nu} = \frac{1}{\sqrt{-g}} (\sqrt{-g} T_t^r)_{,r} = 0.$$

This equation when integrated give us the negative of the energy flux,

$$4\pi H_\theta r^2 [(e+p)u^r u_t] = -\dot{E}. \quad (15)$$

The relativistic Bernoulli equation is obtained by combining equations (12) and (15),

$$\mathcal{E} = \frac{\dot{E}}{\dot{M}} = -hu_t = \text{constant}, \quad (16)$$

Here, $u_t = \sqrt{1/(1 - \omega_\phi \lambda)} \alpha \gamma$, where $\gamma = \gamma_v \gamma_\phi$ is the total bulk Lorentz factor, $\gamma_\phi = 1/\sqrt{1 - \Omega \lambda}$ is the bulk azimuthal Lorentz factor and $\gamma_v = 1/\sqrt{1 - v^2}$ is the bulk radial Lorentz factor. Moreover, $\alpha^2 = (r^2 \Delta)/A$ and $\omega_\phi = -g_{t\phi}/g_{\phi\phi}$. The angular velocity is $\Omega = u^\phi/u^t$.

We simplify equation (9) with the help of equations (4), (11), (12) and (6) and get derivative of bulk velocity,

$$\frac{dv}{dr} = \frac{\mathcal{N}}{\mathcal{D}}, \quad (17)$$

where

$$\begin{aligned} \mathcal{N} &= 2Na^2 \{(2N+1)\Delta\}^{-1} (1 - a_s^2/r) - A(r^4 \Delta)^{-1} \\ &\quad - A\gamma_\phi^2 (r^2 \Delta)^{-1} (1 - w_\phi \lambda) \frac{\Omega^2}{\alpha^2} \left[\frac{A}{r^4} - \alpha^2 \left(r - \frac{a_s^2}{r^2} \right) \right] \\ &\quad + \gamma_\phi^2 (1 - w_\phi \lambda) \frac{\Omega}{\alpha^2} \frac{2a_s}{r^2 \Delta} \left[\frac{A}{r^3} + \Delta \right] + \frac{2a_s \lambda}{r^3 \Delta} \gamma_\phi^2 \\ &\quad + \frac{Na^2}{(2N+1)} \left[\frac{5}{r} - \frac{1}{\mathcal{F}} \frac{d\mathcal{F}}{dr} \right] \end{aligned}$$

and

$$\mathcal{D} = \frac{\gamma_v^2}{v} \left[v^2 - \frac{2Na^2}{(2N+1)} \right].$$

And from equations (4), we get derivative of dimensionless temperature,

$$\frac{d\Theta}{dr} = -\frac{2\Theta}{(2N+1)} \left[\frac{1}{\Delta} \left(1 - \frac{a_s^2}{r} \right) + \frac{\gamma_v^2}{v} \frac{dv}{dr} + \frac{5}{2r} - \frac{1}{2\mathcal{F}} \frac{d\mathcal{F}}{dr} \right], \quad (18)$$

where $\frac{1}{\mathcal{F}} \frac{d\mathcal{F}}{dr} = \frac{\lambda \gamma_\phi^2}{(A - 2a_s r \lambda)} \left[2(\lambda - a_s) - \Omega(A' - 2A/r + 2a_s \lambda) \right] + \frac{A' + 3\Delta' a_s^2}{A + 3\Delta a_s^2} - \frac{A'}{A}$, $A' = 4r^3 + 2ra_s^2 + 2a_s^2$ and $\Delta' = 2(r-1)$.

2.2.1 Accretion critical points

BH accretion is necessarily transonic because the inner boundary condition is always supersonic. At $r \rightarrow r_c$ the

critical point, $dv/dr \rightarrow 0/0$, which gives the critical point conditions,

$$\mathcal{N} = 0 \implies v_c^2 = \frac{\frac{A_c}{r_c^4 \Delta_c} + N_u}{\frac{1}{\Delta_c} \left(1 - \frac{a_s^2}{r_c^2}\right) + \frac{5}{2r_c} - \frac{1}{2\mathcal{F}_c} \frac{d\mathcal{F}_c}{dr}}, \quad (19)$$

$$N_u = \frac{A_c \gamma_{\phi c}^2}{r_c^2 \Delta_c} (1 - w_{\phi c} \lambda) \frac{\Omega_c^2}{\alpha_c^2} \left[\frac{A_c}{r_c^4} - \alpha_c^2 \left(r_c - \frac{a_s^2}{r_c^2} \right) \right] - \gamma_{\phi c}^2 (1 - w_{\phi c} \lambda) \frac{\Omega_c}{\alpha_c^2} \frac{2a_s}{r_c^2 \Delta_c} \left[\frac{A_c}{r_c^3} + \Delta_c \right] - \frac{2a_s \lambda}{r_c^3 \Delta_c} \gamma_{\phi c}^2$$

and

$$\mathcal{D} = 0 \implies v_c^2 = \frac{2N_c a_c^2}{2N_c + 1}, \quad (20)$$

where subscript ‘c’ denotes a flow variable at critical point. The gradient of velocity at r_c is obtained by L’Hôpital’s rule. Relativistic Bernoulli parameter (equation 16) at critical point is written as

$$\mathcal{E} = -hu_t = -h_c u_{tc} = h_c \alpha_c \frac{\sqrt{1/(1 - w_{\phi c} \lambda)}}{\sqrt{(1 - v_c^2)(1 - \Omega_c \lambda)}}, \quad (21)$$

Solving equations (19)–(21) together, we find that for a given set of parameters (\mathcal{E} , λ , ξ and a_s), flow may have single or two to three critical points. In case there are three critical points, then the inner (r_{ci}) and outer (r_{co}) critical points are of saddle type (or X -type) and middle (r_{cm}) is of the centre type (O -type). Therefore, the accretion solutions, which come from infinity, on to the BH horizon, can pass only through r_{ci} or r_{co} or both critical points when shock transition occurs (Fukue 1987).

2.3 Equations of motion for jets

Although the general form of jet equations of motion is the same as that of the accretion disc (equation 2), the flow geometry is entirely different. The accretion disc occupies the space around the equatorial plane ($\theta = \pi/2$), but the jet flows about the axis of symmetry. Therefore, none of the three-velocity components of the jet are negligible. If we define the coordinate velocities and respective momentum per inertial mass as (Chakrabarti 1985)

$$\vartheta_j^i = \frac{u_j^i}{u_j^t} \quad \text{and} \quad \vartheta_{ij} = -\frac{u_{ij}}{u_{it}}, \quad (22)$$

where indices $i = (r, \theta, \phi)$ and subscript ‘j’ represents the quantities for the jet flow. The azimuthal three-velocity of the jet $v_\phi^2 = \vartheta_{\phi j} \vartheta_j^\phi$ will be orthogonal to the stream line, and the advection three-velocity $v_p^2 = \vartheta_{rj} \vartheta_j^r + \vartheta_{\theta j} \vartheta_j^\theta$ will be along

the streamline. Here, the jet angular velocity and specific angular momentum are defined as $\Omega_j = \vartheta_j^\phi$ and $\lambda_j = \vartheta_{\phi j}$, respectively. Above the equatorial plane the constant angular momentum surface is the VZS, which are also the surfaces of constant entropy. VZS is characterized by von Zeipel parameter given by Kozłowski et. al. (1978) and Chakrabarti (1985),

$$Z_\phi^2 = \frac{\vartheta_{\phi j}}{\vartheta_j^\phi} = \left[\frac{A_j - 2a_s r_j \lambda_j}{\Delta_j - a_s^2 \sin^2 \theta_j + 2a_s r_j \sin^2 \theta_j / \lambda_j} \right] \sin^2 \theta_j, \quad (23)$$

where A_j , a_s , and Δ_j are the properties of the metric (see equation 5), applied to the jet. Chakrabarti (1985) showed that in order to obtain the streamline, the following relation should hold,

$$\vartheta_{\phi j} = c_\phi Z_\phi^{n_c}, \quad (24)$$

where c_ϕ and n_c are some constant parameters. Chattopadhyay & Kumar (2016) connected these jet streamlines with the accretion disc, where, n_c and c_ϕ were determined from the accretion disc properties. If r_{sh} is the location of shock and r_{ci} is the inner sonic point of the accretion disc, then the radius of jet base on the equatorial plane is $x_b = (r_{ci} + r_{sh})/2$, and the polar angle of the jet base on the disc surface is $\theta_b = \tan^{-1}(x_b/H_b)$, where H_b is the disc height at x_b . Then the radius of the jet base is $r_b = x_b \text{cosec} \theta_b$. The cross-section area of jet, orthogonal to the jet streamline at r_j is given by

$$A_j = \mathcal{A}_b \left(\frac{r_j}{r_b} \right)^2 \sin \theta_j, \quad (25)$$

where $\mathcal{A}_b = \mathcal{A}'_b \sin \theta_b$ and $\mathcal{A}'_b = 2\pi(r_{b0}^2 - r_{bi}^2)$. Here, $r_{bi} = r_{ci}/\sin \theta_b$, $r_{b0} = r_{sh}/\sin \theta_b$. And, θ_j is defined in Appendix A. If the equations of motion of the jet are integrated along the streamline (equation 24), along with the EoS (equation 6) and equations (23) and (24), a constant of motion that is similar to the Bernoulli parameter is obtained,

$$\mathcal{R}_j = -h_j u_{tj} [1 - c_\phi^2 Z_\phi^{(2n_c - 2)}]^\beta = \mathcal{E}_j [1 - c_\phi^2 Z_\phi^{(2n_c - 2)}]^\beta = \mathcal{B}_j \gamma_j^{(1 - 2\beta)}. \quad (26)$$

Here, $u_{tj} = -\sqrt{1/(1 - \omega_{\phi j} \lambda_j)} \alpha_j \gamma_j$, $\alpha_j = (\Delta_j \Sigma_j)/(A_j \sin^2 \theta_j)$, $\gamma_j = \gamma_{vj} \gamma_{\phi j}$, $\gamma_{vj} = 1/\sqrt{1 - v_j}$, $\gamma_{\phi j} = 1/\sqrt{1 - c_\phi^2 Z_\phi^{(2n_c - 2)}}$, $\beta = n_c/(2n_c - 2)$, \mathcal{E}_j is the jet Bernoulli parameter and the jet velocity measured in corotating frame is $v_j = \gamma_{\phi j} v_p$ (see Lu 1985, for definition). In equation (26), \mathcal{B}_j is the effective

Bernoulli parameter, obtained after extracting all the $\gamma_{\phi j}$ terms from the expression of \mathcal{R}_j .

Integral form of continuity equation gives mass outflow expression along the streamline that can be written as

$$\dot{M}_o = \rho_j u_j^p \mathcal{A}_j, \quad (27)$$

where $u_j^p = \sqrt{g^{pp}} \gamma_{vj} v_j$ is the jet four-velocity parallel to the jet stream line, ρ_j is the mass density and \mathcal{A}_j is the area of the jet cross-section orthogonal to the streamline, respectively. The $g^{pp} = 1/h_p^2$ is defined in Appendix A. Similar to the entropy-accretion rate equation, we can also define the entropy-outflow rate for the jet flow,

$$\dot{\mathcal{M}}_j = u_j^p \mathcal{A}_j e^{k_3} \Theta_j^{3/2} (3\Theta_j + 2)^{k_1} (3\Theta_j + 2/\chi)^{k_2}, \quad (28)$$

This entropy-outflow rate quantity is also constant along the jet streamline except at the shock.

The differential form of equations (26) and (27) with the help of equation (13) can be expressed as derivatives of jet velocity and dimensionless temperature,

$$\frac{dv_j}{dr_j} = \frac{\mathcal{N}_j}{\mathcal{D}_j} = \frac{a_j^2 (\mathcal{A}_j)^{-1} d\mathcal{A}_j/dr_j - a_j^2 h_p^{-1} dh_p/dr_j - X_g}{v_j \gamma_{vj}^2 [1 - a_j^2/v_j^2]}, \quad (29)$$

and

$$\frac{d\Theta_j}{dr_j} = -\frac{\Theta_j}{N_j} \left[\frac{\gamma_{vj}^2}{v_j} \frac{dv_j}{dr_j} + \frac{1}{\mathcal{A}_j} \frac{d\mathcal{A}_j}{dr_j} - \frac{1}{h_p} \frac{dh_p}{dr_j} \right], \quad (30)$$

where

$$X_g = \frac{0.5}{(g_{tt} + w_\phi g_{t\phi})} \left[\frac{dg_{tt}}{dr_j} + \frac{d(w_\phi g_{t\phi})}{dr_j} \right] + \frac{\lambda_j}{2(1 - w_\phi \lambda_j)} \frac{dw_\phi}{dr_j}.$$

If we compare the jet equation in the present paper with radial outflow equations around Schwarzschild metric, then by making transformations such as $u_j^p \rightarrow u^r$, $\mathcal{A}_j^{-1} d\mathcal{A}_j/dr_j \rightarrow 2/r$, $h_p \rightarrow h_r$, we will be able to transform equation (29) to equation 7a of [Chattopadhyay & Ryu \(2009\)](#). This allows us to identify the first term of \mathcal{N}_j as the coupling between cross-section and the thermal term, the second one being the coupling between gravity and the thermal term and the third term or X_g as purely the gravity term.

2.3.1 Jet critical points

Similar to accretion critical points, we can also find jet critical points by using $\mathcal{N}_j = \mathcal{D}_j = 0$, which gives two critical point conditions and they are

$$v_{jc} = a_{jc} \quad \text{and} \quad v_{jc} = \sqrt{\frac{X_g}{\mathcal{A}_{jc}^{-1} d\mathcal{A}_{jc}/dr_{jc} - h_p^{-1} dh_p/dr_{jc}}} \quad (31)$$

At the jet sonic point, i. e. r_{jc} , the gradient of velocity is determined by L'Hôpital's rule.

2.4 Shock waves in accretion and bipolar jets

It has been shown previously that accretion disc shock may launch bipolar jets ([Molteni et al. 1994, 1996a,b](#); [Das et al. 2014](#); [Lee et al. 2016](#)). The jump condition across an accretion shock is obtained by conserving fluxes across the shock front, e.g., mass flux, momentum flux and energy flux ([Taub 1948](#)). In the presence of mass-loss at the shock, mathematically they are

$$\dot{M}_+ = \dot{M}_- - \dot{M}_o = \dot{M}_- (1 - R_m), \quad (32)$$

where $R_m = \dot{M}_o/\dot{M}_-$ is the relative mass outflow rate,

$$H_+ \rho_+ h_+ \gamma_{v_+}^2 v_+^2 + p_+ H_+ = H_- \rho_- h_- \gamma_{v_-}^2 v_-^2 + p_- H_-, \quad (33)$$

and

$$\mathcal{E}_+ = \mathcal{E}_-. \quad (34)$$

Here, subscripts ‘-’ and ‘+’ are representing flow quantities before and after shock transition, respectively. Now, we have solved three shock conditions (32)–(34) simultaneously, where angular momentum is continuous across the shock and we get the relation between pre-shock and post-shock flow variables as

$$h'_- u_-^2 - k_1 u_- + 2\Theta_- = 0 \quad \text{and} \quad k_2 - h'_- \gamma_{v_-} = 0, \quad (35)$$

where $k_1 = (1 - R_m)(h'_+ u_+^2 + 2\Theta_+)/u_+$, $k_2 = h'_+ \gamma_{v_+}$, $h'_\pm = (f_\pm + 2\Theta_\pm)$ and $u = v\gamma_v$. The explicit expression of relative mass outflow rate was defined with the help of equations (12), (25) and (27) in terms of post-shock flow variables and jet base quantities and is written as ([Chattopadhyay & Kumar 2016](#))

$$R_m = \frac{\dot{M}_o}{\dot{M}_-} = \frac{1}{\left[(4\pi H_+ r_+ \rho_+ u_+^r) / (\mathcal{A}_{jb} \rho_{jb} u_{jb}^p) + 1 \right]} = \frac{1}{\left[\Sigma (R_A R_\Xi)^{-1} + 1 \right]},$$

where $\rho_{jb} = \rho_b \exp(-7x_b/(3h_b))/h_b^2$, $u_{jb}^p = \sqrt{g^{pp}} \gamma_{vb} v_{jb}$ and $\mathcal{A}_{jb} = \mathcal{A}_b \sin\theta_b$ are the jet base density, the four-velocity at jet base and the cross-section area of jet base, respectively. Moreover, $R_A = \mathcal{A}_{jb}/(4\pi H_+ r_+)$, $R = (u_-^r)/(u_+^r)$ the compression ratio, $\Sigma = \rho_+/\rho_-$ the density jump across the

accretion shock and $\Xi = (\rho_{\text{jb}} u_{\text{jb}}^p) / (\rho_- u_-^r)$ the ratio of the relativistic mass flux of the jet base to the pre-shock accretion flow, respectively. Therefore, $R_{\dot{m}}$ will increase with increasing R , R_A and Ξ , but will decrease with increasing Σ .

2.4.1 Shock in jets

Parallel to conservation of fluxes of conserved quantities in accretion disc, we can also conserve the fluxes of jet flows along the streamline to obtain shock conditions,

$$[\dot{M}_o] = 0, \quad [\rho_j h_j \gamma_{o_j}^2 v_j^2 + p_j] = 0 \quad \text{and} \quad [\mathcal{R}_j] = 0 \quad (36)$$

3 SOLUTION PROCEDURE

In this paper, we obtain accretion-jet solutions self-consistently, similar to our previous effort in Schwarzschild metric (Chattopadhyay & Kumar 2016), but now for Kerr metric. Recently, we showed that smooth accretion solutions do not automatically drive bipolar jets, while shocked accretion may drive jet from the PSD (Lee *et al.* 2016). Therefore, we look for shocked accretion solution. Once we obtain shocked accretion solution, then we search for the transonic jet solutions. Moreover, we also check for shocks in jets. In the following, for a given a_s and ξ , we list the exact methodology to obtain the accretion-jet solution.

(i) We supply \mathcal{E} and λ in equation (21) and with the help of critical point conditions (equations 19 and 20) we obtain the critical points of the flow. In a significant part of the \mathcal{E} — λ parameter space, multiple critical points (MCP) are possible.

(ii) We determine the gradient of v at the critical point by employing L'Hôpital's rule. Then starting from the critical points we integrate equations (17) and (18) to obtain the solutions.

(iii) For those \mathcal{E} and λ that admit MCP, the entropy at each such point is checked. If the entropy at r_{co} $\dot{\mathcal{M}}_{\text{co}}$ is less than $\dot{\mathcal{M}}_{\text{ci}}$ at r_{ci} , then we check for shock jump (equation 35) considering $R_{\dot{m}} = 0$. If there is a shock, supersonic flow

through r_{co} jumps to the subsonic branch, which ultimately becomes transonic at r_{ci} and falls into the BH as supersonic flow.

(iv) Once the shock in accretion r_{sh} is found, we assume the base of the jet streamline to be at $r_b = (r_{\text{ci}} + r_{\text{sh}})/2$. At r_b , we compute \mathcal{R}_j of the jet from the disc values of \mathcal{E} and γ_ϕ and a guess value of n_c . We then evaluate the von Zeipel parameter (equation 23), as we did for the Schwarzschild case (Chattopadhyay & Kumar 2016), but now for Kerr metric. And then using these values we look for transonic jet solution. We iterate c_ϕ and n_c for the same values of Z_ϕ and r_b and by estimating the value of \mathcal{R}_j from the disc. This goes on until the entropy of the transonic jet is in between the PSD and pre-shock disc or $\dot{\mathcal{M}}_{r_{\text{ci}}} > \dot{\mathcal{M}}_j > \dot{\mathcal{M}}_{r_{\text{co}}}$.

(v) Once the transonic solution is found, then from Section 2.4, we compute the $R_{\dot{m}}$, which is fed to equation (35) to recalculate the r_{sh} . Once the new r_{sh} is obtained, steps (iii)–(v) are repeated but with the new value of $R_{\dot{m}}$, till r_{sh} converges to a value. The resulting jet is the self-consistent jet solution driven by disc properties.

(vi) While the jet solution is being obtained, shock transition in jets is also studied.

4 RESULTS

We are connecting two flows, namely accretion and jet, and since both the flows are quite complicated, we would first present all possible advective accretion solutions, then all possible jet solutions and then self-consistent accretion-jet solutions.

4.1 Accretion

In this section, we present only accretion solution, i. e. we follow steps (i)–(iii) of Section 3. BH accretion disc is necessarily transonic, i. e. the solutions falling on to a BH passes through atleast one sonic point. Therefore, a lot of insight can be gained by studying the critical point conditions. For a given value of \mathcal{E} and λ , the critical points can be uniquely determined. Let us denote $\mathcal{E}_c = \mathcal{E}|_{r_c}$ and $\dot{\mathcal{M}}_c = \dot{\mathcal{M}}|_{r_c}$. Therefore, using the critical point conditions (equations 19 and 20) in equation(16), we obtain energy as a function of r_c for

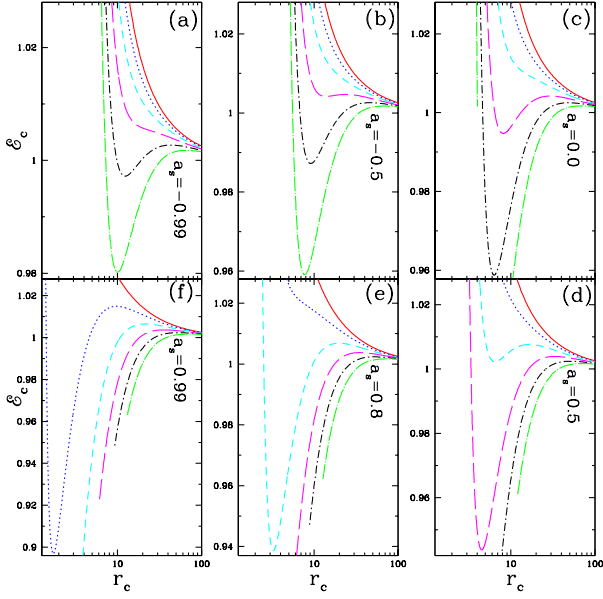


Figure 1. Accretion disc critical point properties: \mathcal{E}_c as a function of critical point r_c for different Kerr spin parameters, $a_s = -0.99$ (a), $a_s = -0.5$ (b), $a_s = 0.0$ (c), $a_s = 0.5$ (d), $a_s = 0.8$ (e) and $a_s = 0.99$ (f). Each of the curves from top to bottom is for $\lambda = 1.5 - 4.0$ with interval $d\lambda = 0.5$. All curves are for the same composition parameter, $\xi = 1.0$ or e - p flow.

given values of λ , a_s and ξ (equation 21). We plot \mathcal{E}_c with r_c for $a_s = -0.99$ (Fig.1a), $a_s = -0.5$ (Fig.1b), $a_s = 0.0$ (Fig.1c), $a_s = 0.5$ (Fig.1d), $a_s = 0.8$ (Fig.1e) and $a_s = 0.99$ (Fig.1f). Each of the curves plotted from top to bottom is for $\lambda = 1.5 - 4.0$ with interval $d\lambda = 0.5$ and with same composition parameter, $\xi = 1.0$. Critical points are formed because gravity increases the infall velocity, but because accretion is an example of convergent flow the temperature of the flow also increases during accretion (compressional heating). As temperature increases, sound speed also increases, but in accretion the rise of sound speed is less than the bulk velocity. Therefore, the flow that is subsonic at large distances becomes supersonic within a certain point (critical point). However, if the infalling matter is rotating, then the centrifugal term competes with the gravitation term in a way that MCP may form. As a_s increases, frame dragging enhances the centrifugal term significantly, therefore, even matter with low angular momentum exhibits MCP, for example, the flow with $\lambda = 2$ [dotted in Figs. 1a-f] exhibits MCP for $a_s = 0.99$ but not for $a_s \leq 0.8$. On the other hand, if the flow is retrograde, then MCP occur only for higher angular momentum flow. Fig. (1c) is similar to fig. 3a of

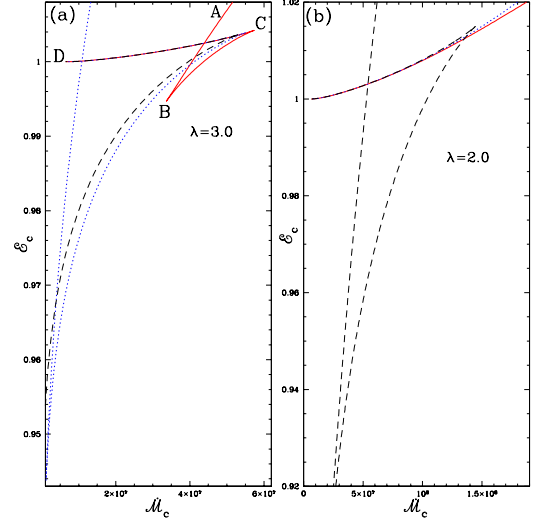


Figure 2. Accretion disc critical point properties: \mathcal{E}_c versus \dot{M}_c ; each curve plotted for Kerr parameters, $a_s = 0$ (solid, red), $a_s = 0.5$ (dotted, blue), $a_s = 0.99$ (dashed, black). (a) Angular momentum $\lambda = 3$ (b) $\lambda = 2$. All curves are for the same composition parameter, $\xi = 1.0$ or e - p flow.

Chattopadhyay & Chakrabarti (2011). This phenomenon is better exhibited with $\mathcal{E}_c - \dot{M}_c$ ‘kite-tail’ plot.

For a given set of \mathcal{E} and λ , there can be one to three critical points. In general, when MCP occur for a given set of \mathcal{E} & λ , then each of the critical points possesses different entropy from the other. In $\mathcal{E}_c - \dot{M}_c$ (i.e. evaluated at critical points) for a given λ , the curve takes the shape of a kite-tail. In Fig. 2(a), we plot \mathcal{E}_c versus \dot{M}_c curves for $a_s = 0$ (solid, red), $a_s = 0.5$ (dotted, blue) and $a_s = 0.99$ (dashed, black) all the curves for the same angular momentum $\lambda = 3.0$. Branch AB (marked on the curve related to $a_s = 0$) corresponds to r_{ci} , BC corresponds to r_{cm} and CD to r_{co} . This implies that, for a given λ , there is a range of \mathcal{E} and \dot{M} for which MCP may form. As we opt for higher spin of the BH (dotted, dashed), the MCP region shifts to the lower entropy region. And for highly spinning BH, for example $a_s = 0.99$, the inner critical point (r_{ci}) does not form. In contrast, for flows with lower λ ($= 2$), MCP form for highly spinning BH like $a_s = 0.99$. But for lower a_s , accretion flows with low λ form only r_{co} -type sonic points (Fig. 2b). Interestingly, Figs. (2a) and (b) show that, for a given \mathcal{E}_c and \dot{M}_c , the outer sonic points or r_{co} are formed at roughly the same location in accretion discs around BHs of different a_s , but the locations of r_{cm} and r_{ci} differ widely.

In Fig. 3, we divide the $\mathcal{E} - \lambda$ parameter space into

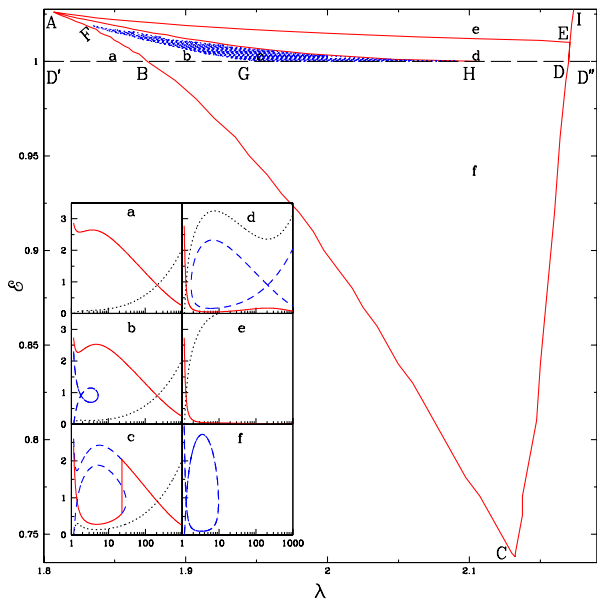


Figure 3. Accretion disc: $\mathcal{E} - \lambda$ parameter space, showing single sonic point, MCP and shock region, with typical solutions from each region (panels a–f). The BH is of spin $a_s = 0.99$. The composition parameter is $\xi = 1.0$ or $e - p$ flow.

regions that will admit single critical points and MCP and shocks for accretion flows around a Kerr BH of $a_s = 0.99$. In the region ABD' the angular momentum is low and solutions in this domain will possess a single outer-type critical point (typical solution Mach number $M = v/a$ versus r : panel a). In the region $ABHA$, the angular momentum is higher and three sonic points (r_{ci} , r_{cm} , r_{co}) appear, although the flow still passes through r_{co} on to the BH (typical solution in panel b). The shaded region $FGHF$ represents flow parameters for which steady-state shocks are possible. In other words, matter with parameters from the region $FGHF$ flows through r_{co} , becomes subsonic at the shock location r_{sh} and finally enters the BH through r_{ci} (typical solution in panel c). Solutions from the region $AHDEA$ are also characterized by three sonic points, but since the entropy $\dot{\mathcal{M}}_i$ of the inner critical point is higher than that of the outer critical point, so the matter flows into the BH through r_{ci} (typical solution in panel d). The parameters from the region above AEI have very high angular momentum such that it becomes transonic close to the horizon producing a single inner-type critical point r_{ci} . These solutions are monotonic and smooth functions of r (typical solution in panel e). Solutions from the region $BDCB$ are bound and do not produce global solution (typical solution in panel f). Parameters from the rest

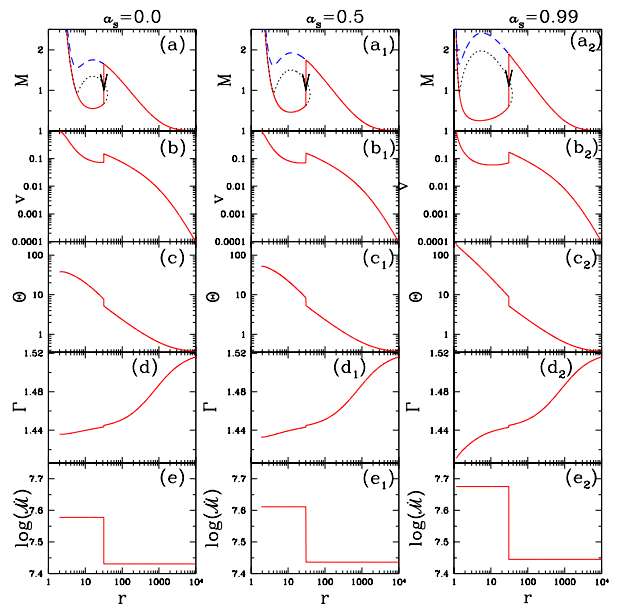


Figure 4. Accretion disc: M (a, a_1 , a_2), v (b, b_1 , b_2), Θ (c, c_1 , c_2), Γ (d, d_1 , d_2) and $\dot{\mathcal{M}}$ (e, e_1 , e_2) are plotted with r along the equatorial plane. Accretion on to a BH of $a_s = 0.0$ is for $\lambda = 3.05$ (a–e); those on to a BH of $a_s = 0.5$ are for $\lambda = 2.716$ ($a_1 - e_1$) and flows on to a BH with $a_s = 0.99$ are plotted for $\lambda = 2.01$ ($a_2 - e_2$). For all plots $\mathcal{E} = 1.001$ and $\xi = 1.0$ and the shock location is at $r_{sh} = 30.40$. Arrows on vertical lines show the shock jump (a, a_1 , a_2).

of the region do not produce transonic solutions that connect the horizon. The solid curves in panels above are the physical solutions. The dotted curves are solutions for the wind-type boundary condition and the dashed curves represent possible accretion solutions but that are not chosen by the matter.

We now compare shocked accretion disc solutions around BHs of three Kerr parameters $a_s = 0$ (Figs. 4a–e), $a_s = 0.5$ (Figs. 4a₁ – e₁), $a_s = 0.99$ (Figs. 4a₂ – e₂), where the flow angular momenta are 3.05, 2.716 and 2.01, respectively. All the three cases presented above have same energy $\mathcal{E} = 1.001$. The flow variables plotted as a function of r are the Mach number M (Figs. 4a–a₂), v (Figs. 4b–b₂), Θ (Figs. 4c–c₂), Γ (Figs. 4d–d₂) and $\log(\dot{\mathcal{M}})$ (Figs. 4e–e₂). The most interesting thing is that the shock formed in all the three cases is exactly at $r_{sh} = 30.2$. In other words, accretion discs around BHs of different spin may form shock at the same radial distance, if the angular momenta of the discs are different even if \mathcal{E} remains the same. Although r_{sh} has the same value, the flow variables at any given r are different for accretion discs around BHs of different a_s . As an

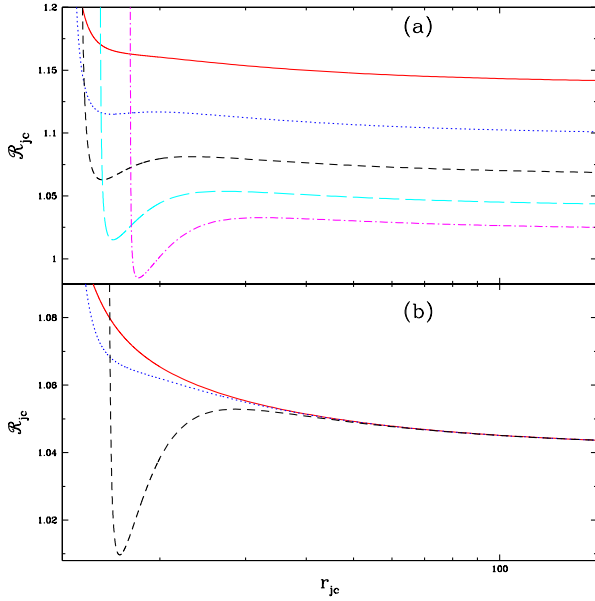


Figure 5. Jet: \mathcal{R}_{jc} as a function of critical points r_{jc} for a given BH spin $a_s = 0.9$ (a) and for a given flow angular momentum $\lambda_j = 2$ (b). (a) Each curve represents $\lambda_j = 3.5$ (solid, red), $\lambda_j = 3.0$ (dotted, blue), $\lambda_j = 2.5$ (dashed, black), $\lambda_j = 2.0$ (long-dashed, cyan) and $\lambda_j = 1.5$ (dash-dotted, magenta). (b) Each curve represents $a_s = 0.0$ (solid, red), $a_s = 0.5$ (dotted, blue) and $a_s = 0.99$ (dashed, black). All the figures are plotted for the same von Zeipel parameter, $Z_\phi = 10$ and $n_c = 0.5$.

example, the temperature of the PSD for BH of $a_s = 0.99$ is much higher than that of the flow on to a BH of $a_s = 0$, so radiations computed from such flow would indeed be different, but if r_{sh} is oscillating there is a chance that it would be oscillating at the same frequency.

4.2 All possible jet solutions

In this section, we would like to discuss about all possible jet solutions: in other words, we solve equations (29) and (30) with the help of equation (31), for given values of Z_ϕ (equation 23). Since \mathcal{R}_j is a constant of motion, so we express \mathcal{R}_j in terms of critical point conditions (equation 31) and solve for r_{jc} : we will obtain all possible sonic points. In addition, once we specify Z_ϕ , the jet cross-section is specified and the entire jet solution can be obtained. In this section, \mathcal{R}_j and Z_ϕ are supplied as free parameters, in order to find all possible solutions.

In Fig. (5a), we plot the jet energy parameter \mathcal{R}_{jc} as a function of r_{jc} for flows with $\lambda_j = 3.5$ (solid, red), $\lambda_j = 3.0$ (dotted, blue), $\lambda_j = 2.5$ (dashed, black), $\lambda_j = 2.0$ (long-dashed, cyan) and $\lambda_j = 1.5$ (dash-dotted, magenta)

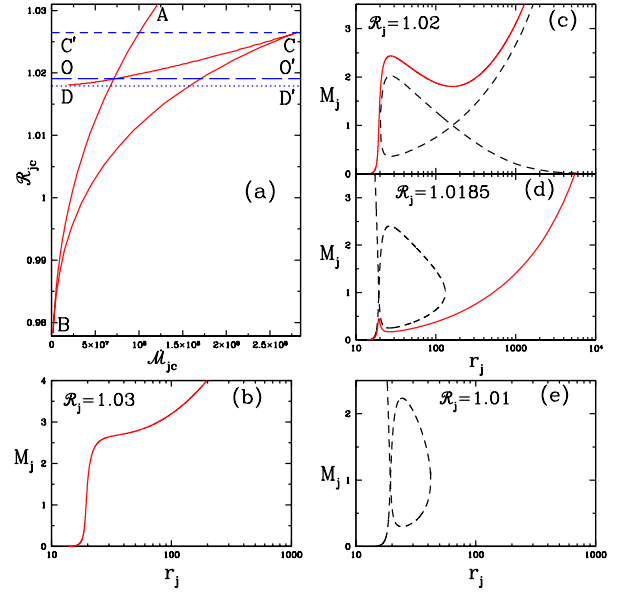


Figure 6. Jet: Variation of (a) \mathcal{R}_{jc} with (\dot{M}_{jc}) for $a_s = 0.99$ (solid, red). Jet Mach number (M_j) with jet stream-line r_j for different jet energy (b) $\mathcal{R}_j = 1.03$, (c) $\mathcal{R}_j = 1.02$, (d) $\mathcal{R}_j = 1.0185$ and (e) $\mathcal{R}_j = 1.01$. Each solution is plotted for $Z_\phi = 10$, $n_c = 0.5$ and $\lambda_j = 2.0$. Solid and dashed curves represents global and closed jet solutions, respectively.

around a BH with spin $a_s = 0.9$. Here, $\mathcal{R}_{jc} = \mathcal{R}_j|_{r_{jc}}$ and $\dot{M}_{jc} = \dot{M}_j|_{r_{jc}}$. It is clear from the above that jets with two different λ_j will have the same \mathcal{R}_j and r_{jc} at the crossing points. However, the entropy (or \dot{M}_{oc}) of the two flows with different λ at the crossing points of Fig. (5a) are not the same. Another curious aspect is that the jet energy parameter $\mathcal{R}_{jc} > 1$ even for $r_{jc} \rightarrow \infty$. Although this is counter-intuitive, this arises due to the property of VZS, where not only λ_j remains constant but $\gamma_{\phi j}$ also remains constant: therefore, $\mathcal{R}_{jc} \rightarrow (\gamma_{\phi j}|_{r_b})^{1-2\beta}$ as $r_{jc} \rightarrow \infty$. Moreover, in direct contrast with accretion critical point properties, except at the crossing points of the curves, \mathcal{R}_{jc} is generally higher for jets with higher λ_j . For example, curve for $\lambda_j = 3.5$ is of higher \mathcal{R}_{jc} than for $\lambda_j = 3.0$ and so on.

In Fig. (5b), we once again plot \mathcal{R}_{jc} as a function of r_{jc} , but this time for the same flow $\lambda = 2$, but falling on to BHs of different spin $a_s = 0.0$ (solid, red), $\lambda = 0.5$ (dotted, blue) and $a_s = 0.99$ (dashed, black). There are no MCP in jets around BHs of lower spin, but space-time around a rotating BH of $a_s = 0.99$ ensures multiple sonic points in jets.

Figure (6a) is the famous kite-tail relation between \mathcal{R}_{jc} and \dot{M}_c for a given value of angular momentum, i. e., $\lambda_j = 2$.

The curve CD represents the values of \mathcal{R}_{jc} and $\dot{\mathcal{M}}_{jc}$ for all possible r_{jco} . Similarly, curves AB and BC represent the values of \mathcal{R}_{jc} and $\dot{\mathcal{M}}_{jc}$ for all possible r_{jci} and r_{jcm} , respectively. Here, the inner, middle and outer jet sonic points are represented by r_{jci} , r_{jcm} and r_{jco} . In Figs. (6b-e), we plot the related jet solutions, i. e., jet Mach number M_j as a function of r_j . Horizontal line OO' (long-dashed) passes through the intersection of AB and CD at $\mathcal{R}_{jc} = 1.0193$, and CC' (dashed) corresponds to highest \mathcal{R}_{jc} ($= 1.0265$) for which MCP are possible. And DD' is lowest \mathcal{R}_{jc} ($= 1.0181$) for which three sonic points are possible. For $\mathcal{R}_{jc} < 1.0181$ only closed jet solutions are possible with only two sonic points r_{jci} and r_{jcm} , but no r_{jco} . And therefore, in Fig. (6b), there is one inner-type critical point since $\mathcal{R}_j = 1.03$ lies above the CC' in \mathcal{R}_{jc} — $\dot{\mathcal{M}}_c$ space. The energy parameter of the jet in Fig. (6c), is $\mathcal{R}_j = 1.02$ which is in between CC' and OO'. In this domain, both r_{jci} and r_{jco} are possible and the entropy of r_{jco} is higher, but the solution (dashed) through r_{jco} is a closed one (dashed), while the one through r_{jci} is global (solid). In Fig. (6d), $\mathcal{R}_j = 1.0185$ lies between OO' and DD', and r_{jci} , r_{jco} still form, but now the global solution (solid) is through r_{jco} and the closed solution is through r_{jci} . It is clear from Fig. (6a), that the inner critical point has higher entropy for solutions with \mathcal{R}_j between OO' and DD'. In Fig. (6e), $\mathcal{R}_j = 1.01$ below DD' possesses a X-type r_{jci} and O-type r_{jcm} . The jet flows out through r_{jci} but turns back around the O-type sonic points, i. e. there is no global solution, only a closed one.

In Fig. (6c), we observe that the jet solution admits multiple critical points. In the case of accretion disc, the gravity ensures one critical point, but if the matter is rotating then centrifugal term modifies the gravitational interaction and forms multiple sonic or critical points. However, in jets the effect of centrifugal term along the streamline is quite small. In Fig. (7a), we plot various terms of the numerator \mathcal{N}_j of equation (29) in order to understand why we have MCP, for the same jet parameters as considered in Fig. (6c). In Fig. (7b), we plot the \mathcal{N}_j for all the branches of the jet solution for $R_j = 1.02$, $\lambda = 2.0$. From equation (29) it is clear that the jet will accelerate ($dv_j/dr_j > 0$) if $\mathcal{N}_j < 0$ in the subsonic ($v_j < a_j$) regime and changes

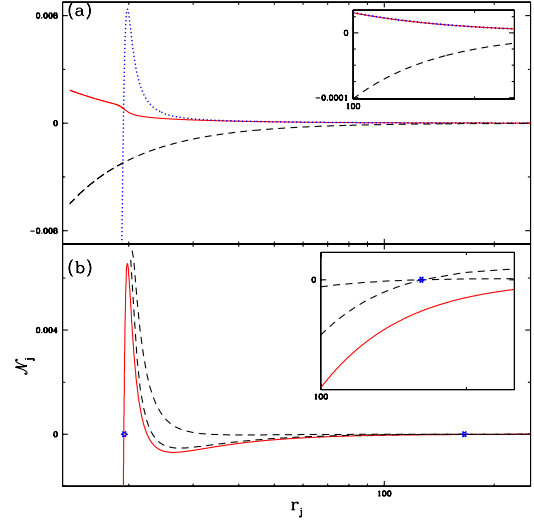


Figure 7. Jet: various terms of \mathcal{N}_j like (a) $a_j^2(\mathcal{A}_j)^{-1}(d\mathcal{A}_j)/(dr_j)$ (solid, red), $-a_j^2 h_p^{-1}(dh_p)/(dr_j)$ (dotted, blue) and $-X_g$ (dashed, black) are plotted with r_j . (b) \mathcal{N}_j for the global solution through r_{jci} (solid, red) and the closed solution through r_{jco} (dashed). Asterisk shows the location of two X-type sonic points. Other parameters $Z_\phi = 10$, $n_c = 0.5$ and $\lambda_j = 2.0$. Same jet solution as in Fig. (6c).

sign in the supersonic regime ($v_j > a_j$). \mathcal{N}_j becomes zero at the critical point. In Fig. (7a), we plot the three components of \mathcal{N}_j , i.e. $\mathcal{N}_{j1} = a_j^2(\mathcal{A}_j)^{-1}(d\mathcal{A}_j)/(dr_j)$ (solid, red), $\mathcal{N}_{j2} = -a_j^2 h_p^{-1}(dh_p)/(dr_j)$ (dotted, blue) and $\mathcal{N}_{j3} = -X_g$ (dashed, black), as a function of r_j . \mathcal{N}_{j1} , the coupling between thermal and the flow geometry term, is positive definite and \mathcal{N}_{j3} , the gravity term, is negative definite. But it is \mathcal{N}_{j2} , the thermal and metric term, which flips sign, that determines the formation of multiple sonic points and eventually shock. Near the base, where the jet is subsonic, Fig. (7a) shows $\mathcal{N}_{j2} < 0$ and dominates both \mathcal{N}_{j1} and \mathcal{N}_{j3} . Therefore, $\mathcal{N}_j < 0$ near the base (Fig. 7b) and this ensures that the jet accelerates in subsonic region. At r_{jci} or the inner critical point, \mathcal{N}_j becomes zero (inner star in Fig. 7b), as \mathcal{N}_{j2} becomes positive enough to negate gravity. Further out, \mathcal{N}_{j2} remains positive and increases up to a short distance, so the jet continues to accelerate. However, \mathcal{N}_{j2} reaches its maximum and starts to decrease rapidly. At $\text{few} \times 10 r_g$, $\mathcal{N}_{j2} \approx \mathcal{N}_{j1} \ll |\mathcal{N}_{j3}|$, which implies that $\mathcal{N}_j < 0$ at large r_j (solid, red in Fig. 7b). Therefore, the global solution of the jet through r_{jci} decelerates, after it becomes supersonic. This resistance to the supersonic flow creates the possibility for the jet to pass through the second saddle-type sonic

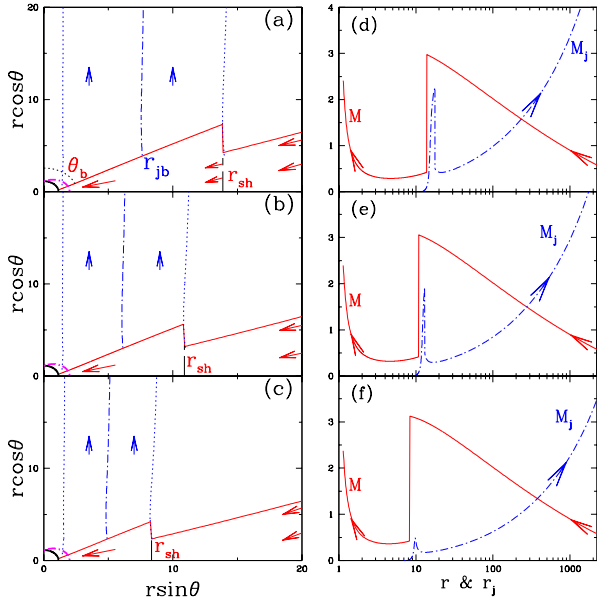


Figure 8. Self-consistent accretion-jet solutions: flow boundary (a, b, c) of accretion disc (solid, red), jet streamline (dash–dotted, blue), jet boundary (dotted, blue), horizon (solid quarter circle), ergosphere (dash–dotted quarter ellipse), the radius of the jet base r_{jb} and its polar angle θ_{jb} are shown. Accretion Mach number M (solid, red) and jet Mach number M_j (dash–dotted blue) with radial distance are plotted (d, e, f). The right-hand panels correspond to the accretion-jet solutions and the left-hand panels correspond to related geometry. Each pair of right- and left-hand panels are plotted for $\lambda = 2$ (a, d), $\lambda = 1.99$ (b, e) and $\lambda = 1.98$ (c, f). Accretion shocks are produced at $r_{sh} = 13.8308$ (a, d), $r_{sh} = 10.8179$ (b, e) and $r_{sh} = 8.2275$ (c, f). The arrows show flow direction. For all the panels $\mathcal{E} = 1.0001$, $\xi = 1.0$ and $a_s = 0.99$.

point. And since the dynamics is forcing the jet to choose another solution, the entropy of the outer critical point is also high. Needless to say, in order to flow out through r_{jco} , the jet has to generate the right amount of entropy via a shock. We plot the \mathcal{N}_j of the solution through the outer sonic point, and one can see that it is positive beyond the outer sonic point (dashed in Fig. 7b). The inset panels in Fig. (7a & b) are plotted to zoom around the outer sonic point (asterisk), to show the different branches of the solution.

4.3 Self-consistent accretion-jet solution

In this section, we present accretion–ejection solutions. We connect Sections 4.1 and 4.2 where the inner boundary condition of the jet is obtained from the PSD, i.e. we follow steps (i)–(v) of Section 3 in totality. In other words, we now obtain simultaneous accretion-jet solutions by supplying accretion disc parameters like \mathcal{E} , λ , flow composition ξ

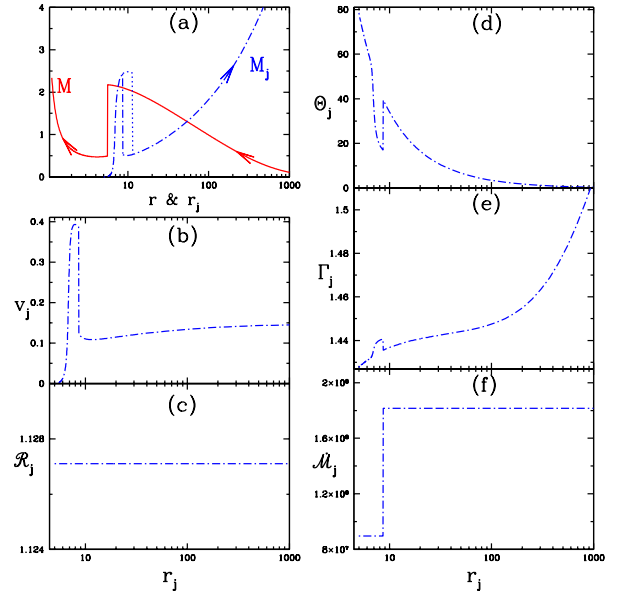


Figure 9. Variations of (a) accretion Mach number M (solid, red) and jet Mach number M_j (dash–dotted, blue) with radial distance on disc equatorial plane r and jet streamline above the equatorial plane, r_j , respectively: Variation of jet flow variables v_j (b), \mathcal{R}_j (c), Θ_j (d), Γ_j (e) and \mathcal{M}_j (f) with r_j . Arrow represents the direction of the flow. Disc parameters are $\mathcal{E} = 1.002$, $\lambda = 1.946$, $\xi = 1.0$ and $a_s = 0.99$. The accretion shock location is at $r_{sh} = 5.9827$. The relative mass outflow rate is $R_{in} = 0.061378$.

and BH spin a_s . In Figs (8a–f), we plot accretion–ejection solutions for same disc specific energy $\mathcal{E} = 1.0001$, but different angular momenta $\lambda = 2.0$ (Figs 8a, d), $\lambda = 1.99$ (Figs 8b, e) and $\lambda = 1.98$ (Figs 8c, f). In the left-hand panels, we plot the disc–jet geometry (Figs 8a–c). In the right-hand panels (Figs 8d–f), we plot accretion disc Mach number M (solid, red) and jet Mach number M_j with distance. M is evaluated on the equatorial plane while M_j along the jet stream line (dash–dotted on the left-hand panels). All the accretion solutions presented here harbour shock, while the top two panels on the right (Figs. 8d & e) show shocks in jets too. The shock in accretion decreases with decreasing λ , and so does the jet cross-section. The jet starts from the surface of the PSD with very low velocity but either expands briskly to become transonic within a short distance and eventually gets shocked, or slowly becomes transonic at a large distance from the central object. In this particular case, the shock strength of the jet is slightly less than that of the accretion disc.

In Fig. (9a), we plot simultaneous accretion and jet Mach numbers M and M_j , respectively, where there are

shocks both in accretion and the jet. In the rest of the figure we plot the jet flow variables like jet three-velocity v_j (Fig. 9b), jet energy parameter R_j (Fig. 9c), Θ_j (Fig. 9d), Γ_j (Fig. 9e) and $\dot{\mathcal{M}}_j$ (Fig. 9e), for the given accretion disc parameters $\mathcal{E} = 1.002$, $\lambda = 1.946$, $\xi = 1.0$ around a BH of $a_s = 0.99$. The mass outflow rate obtained is $R_{\dot{m}} = 0.061378$. The accretion shock is at $r_{\text{sh}} = 5.9827$ on the equatorial plane, while the shock in the jet is at $r_{\text{jsh}} = 8.597$ at $\theta_{\text{jsh}} = 24.64^\circ$. There is another shock location for the jet that is slightly further away (at a distance of 11.448, dotted vertical line), but can be shown to be unstable (Nakayama 1994, 1996). Interestingly, the shock in accretion is at a shorter distance than the shock in jet: therefore, the inner part of the disc–jet system has a complicated structure. The jet starts from the surface of the PSD with almost negligible velocity, is accelerated within a few gravitational radii to about ~ 0.4 , and then jumps down to about ~ 0.1 , and finally its terminal velocity is $v_{j\infty} \sim 0.146$. The jet shock is quite strong (compression ratio ~ 4), and should be a good site for particle acceleration. A major feature of shocks in jets is that the base of the jet is much hotter than the pre-shock portion as well as the post-shock region of the jet. In contrast, PSD is the hottest part of the accretion disc. The jet energy parameter remains constant (Fig. 9c), although the entropy jumps at the shock (Fig. 9e).

In Fig.(10a), we plot accretion disc solutions M (solid, red) and the corresponding jet M_j (dash–dotted, blue) for disc parameters are $\mathcal{E} = 1.0105$, $\lambda = 1.903$, $\xi = 1.0$ and $a_s = 0.99$. The jet velocity v_j (Fig.10b), \mathcal{R}_j (Fig.10c), Θ_j (Fig.10d), Γ_j (Fig.10e) and $\dot{\mathcal{M}}_j$ (Fig.10f). This particular set of disc parameters launches a jet that is free from shock. In this case too, the jet launched by PSD starts with negligible velocity at the base, but rapidly accelerates to become transonic in the next few r_g (Fig.10b), by converting thermal energy into kinetic energy (Fig.10d). Since this jet is shockfree, so in this case the entropy remains constant (Fig.10f) and like the previous case \mathcal{R}_j is constant too. Interestingly, as the jet is rapidly accelerated by thermal gradient term, it reaches a speed $v_j > 0.44$, but eventually the thermal gradient term exhausts itself, and the jet settles to a lesser terminal speed of $v_{j\infty} \sim 0.3525$. The temperature

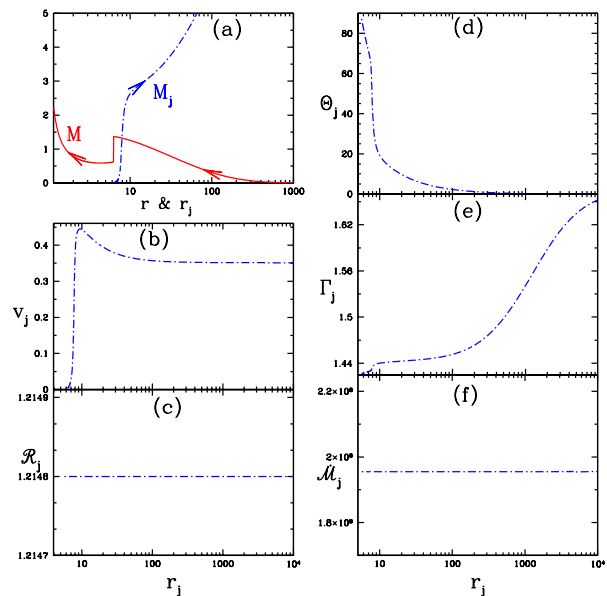


Figure 10. Variations of (a) M (solid, red) and M_j (dash–dotted, blue) with r and r_j , respectively. Variation of v_j (b), \mathcal{R}_j (c), Θ_j (d), Γ_j (e) and $\dot{\mathcal{M}}_j$ (f) with jet streamline r_j . Arrow represents the direction of the flow. Disc parameters are $\mathcal{E} = 1.0105$, $\lambda = 1.903$, $\xi = 1.0$ and $a_s = 0.99$ and accretion shock formed at $r_{\text{sh}} = 6.2941$. The $R_{\dot{m}} = 0.054495$.

drops sharply in the rapid acceleration phase, but at a lesser rate in the region where the jet velocity is approaching an asymptotic value. The jet temperature indeed approaches non-relativistic values at large distances (Fig.10d). This is also shown in the Γ_j variation too (Fig.10e).

In Fig. (11a), we plot the disc shock location r_{sh} with disc angular momentum λ . Each curve is for $\mathcal{E} = 1.0001$ (solid, red), 1.001 (dashed, black) and 1.0019 (long-dashed, magenta). All the curves have fixed values of $a_s = 0.99$ and $\xi = 1.0$. The shock r_{sh} increases with increasing λ at a given \mathcal{E} , as well as increasing \mathcal{E} at a given λ . We plot the related compression ratio R (Fig.11b), jet terminal speed $v_{j\infty}$ (Fig.11c), jet energy parameter \mathcal{R}_j (Fig.11d), the jet shock location r_{jsh} (Fig.11e), effective jet specific energy \mathcal{B}_j (Fig.11f) and $R_{\dot{m}}$ (Fig.11g) with the accretion shock location r_{sh} . The compression ratio R of the shock in accretion disc increases with the decreasing r_{sh} as is shown in Fig. (11b). Compression ratio decreases for weak shock, and for accretion disc shocks, shock becomes weaker as r_{sh} increases. However, only shock compression does not power the jet, and it shows that v_{∞} has a rather complicated dependence on R , where the terminal speed has a clear maximum for

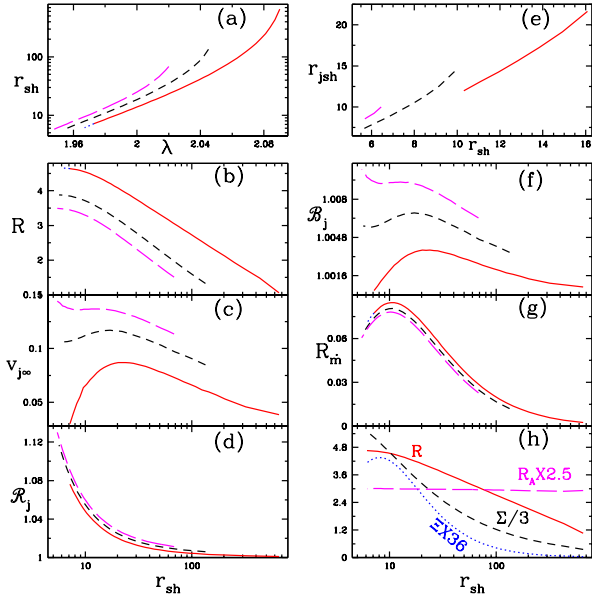


Figure 11. Variations of (a) r_{sh} with λ , and (b) R , (c) $v_{j\infty}$, (d) \mathcal{R}_j , (e) r_{jsh} , (f) \mathcal{B}_j and (g) $R_{\dot{m}}$ with r_{sh} . Each curve is for $\mathcal{E} = 1.0001$ (solid, red), 1.001 (dashed, black) and 1.0019 (long-dashed, magenta). (h) Variation of R (solid), R_A (long-dashed), Σ (dashed) and Ξ (dotted) with r_{sh} for $\mathcal{E} = 1.0001$. For all the panels $\xi = 1.0$ and $a_s = 0.99$.

$\mathcal{E} = 1.0001$ (solid, red), although R decreases with increasing r_{sh} . Moreover, the jet terminal speed is generally higher for higher energies like $\mathcal{E} = 1.00055$ (dashed, black) and $\mathcal{E} = 1.001$ (long-dashed, magenta), although the compression ratio of the accretion shock for such energies is clearly low. Here, $v_{j\infty}$ is not a monotonic function of r_{sh} , but the jet energy parameter \mathcal{R}_j decreases monotonically with increasing r_{sh} (or decreasing R). \mathcal{R}_j is also higher for accretion discs of higher energy. The shock in jet is only formed in a limited range as is shown in Fig. (11e). The shock in jet, i.e. r_{jsh} , increases as disc energy increases: however, the range of steady shock in jet decreases, if the energy of the disc is higher. The relative Bernoulli parameter has similar functional dependence on r_{sh} as $v_{j\infty}$, which is not surprising since at $r \rightarrow \infty$, $\mathcal{B} \rightarrow (1 - v_{j\infty}^2)^{-1/2}$. It is worth noting that the relative mass outflow rate or $R_{\dot{m}}$ does not follow the functional dependence of $v_{j\infty}$ with r_{sh} . $R_{\dot{m}}$ generally increases with decreasing r_{sh} , but also decreases for very small value of r_{sh} , maximizing at some intermediate values of r_{sh} . This is because $v_{j\infty}$ only depends on the \mathcal{B}_j , but $R_{\dot{m}}$ depends on many factors as shown in Section 2.4). In order to understand how $R_{\dot{m}}$ depends on r_{sh} , in the next panel we

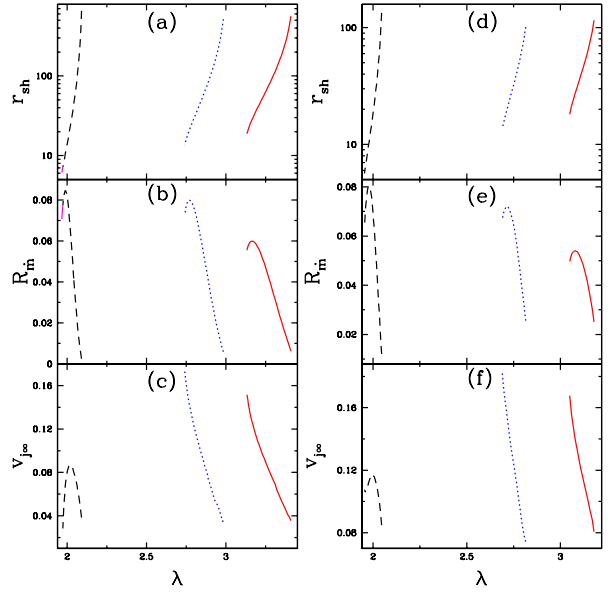


Figure 12. Variations of r_{sh} (a, d), $R_{\dot{m}}$ (b, e) and $v_{j\infty}$ (c, f) with λ are plotted for different BHs of Kerr parameter $a_s = 0.0$ (solid, red), 0.5 (dotted, blue) and 0.99 (dashed, black). The disc parameters are $\mathcal{E} = 1.0001$ (a, b, c) and $\mathcal{E} = 1.001$ (d, e, f). The flow composition for all the plots is $\xi = 1.0$.

analyse only the case presented in this figure, i.e. the case for $\mathcal{E} = 1.0001$ (solid, red in Figs. 11a-g). In Fig. (11h), we plot the accretion compression ratio R (solid, red), the ratio of jet cross-section at the base to the PSD, i.e. R_A (long-dashed, magenta), density contrast across accretion shock, i.e. Σ (dashed, black) and Ξ (dotted, blue) which is the ratio of the relativistic mass flux at the jet base to that of the pre-shock accretion disc: it gives a measure of the upward thrust that the shock generates. From Section 2.4, it is clear that if Σ increases together with the decrease of R_A , R and Ξ , then $R_{\dot{m}}$ will decrease too and vice versa. As r_{sh} decreases by changing λ for $\mathcal{E} = 1.0001$, Σ monotonically increases, R increases but tends to taper off for small r_{sh} , Ξ increases but starts to dip for small r_{sh} and R_A do not change much. Therefore, $R_{\dot{m}}$ generally increases for decreasing r_{sh} , but dips for small values of r_{sh} , which points to the fact that the combined effect of R and Ξ somewhat negates the effect of Σ in determining the value of $R_{\dot{m}}$.

In Fig.(12), we study the dependence of accretion shock r_{sh} (Figs. 12 a, d), the relative outflow rate $R_{\dot{m}}$ (Figs. 12 b, e) and the jet terminal speed $v_{j\infty}$ (Figs. 12 c, f) with the angular momentum λ of the accretion disc. Each curve represents BHs of spin $a_s = 0.0$ (solid, red), 0.5 (dotted, blue)

and 0.99 (dashed, black). The figures on the left-hand panels (Figs. 12 a–c) are plotted for disc energy $\mathcal{E} = 1.0001$ and those on the right-hand panels (Figs. 12 d–f) are plotted for $\mathcal{E} = 1.001$. In the top panels, we show how disc property like r_{sh} depends on disc parameter, while in the middle and bottom panels, we show how jet properties like R_{in} and $v_{\text{j}\infty}$ depend on the disc parameter λ . The accretion shock increases with increasing disc λ for BHs with all possible spins. It is worth noting that accretion shocks may form even for low λ values, if BH spin is high enough (Figs. 12 a and d). Figs. (12a) and (d) vindicate the conclusions of Figs. (4a₁) and (a₂), that accretion shock may occur at the same location, for discs of different λ depending on the spin of the BH. The mass outflow rate from an accretion disc around a highly spinning BH is higher than those around BHs of smaller a_s (Figs. 12 b, e), but R_{in} peaks at intermediate λ for BHs of any given spin. However, $v_{\text{j}\infty}$ for a given disc energy is not necessarily higher for discs around highly spinning BHs, although it tends to increase with the flow energy (Figs. 12 c, f). While, for jets around low- a_s BH, $v_{\text{j}\infty}$ increases monotonically as λ is decreased, but for highly spinning BH, $v_{\text{j}\infty}$ maximizes at intermediate values of λ .

In Fig.(13), we present the \mathcal{E} – λ parameter space of shock in the accretion disc. The region bounded by the solid (black) curve represents \mathcal{E} and λ of the accretion disc that will experience steady shock transition if we ignore the formation of jet. If mass-loss is taken into account, then the region $x_0x_4x_9x_0$ bounded by the dotted (red) curve represents the parameter space for steady accretion shock that launches jet. The region $x_1x_4x_8x_1$ represent the accretion disc parameters for which jets would harbour multiple (two or three) critical points. And the region $x_1x_5x_8x_2$ bounded by dashed (blue) curve represents accretion disc parameters for which the jet possess three critical points. And in the region $x_2x_6x_7x_2$ within long-dashed (magenta) curve, jet launched from the disc undergoes steady shock transition. In the rest of the accretion shock domain (solid, black curve), there is no jet possible. In Fig. (13A), we compare the shock parameter space for BHs with spin parameters $a_s = -0.99, 0.0, 0.5, 0.7, 0.9$. In Fig. (13B), we plot the shock parameter space for $a_s = 0.99$ and in the inset panels,

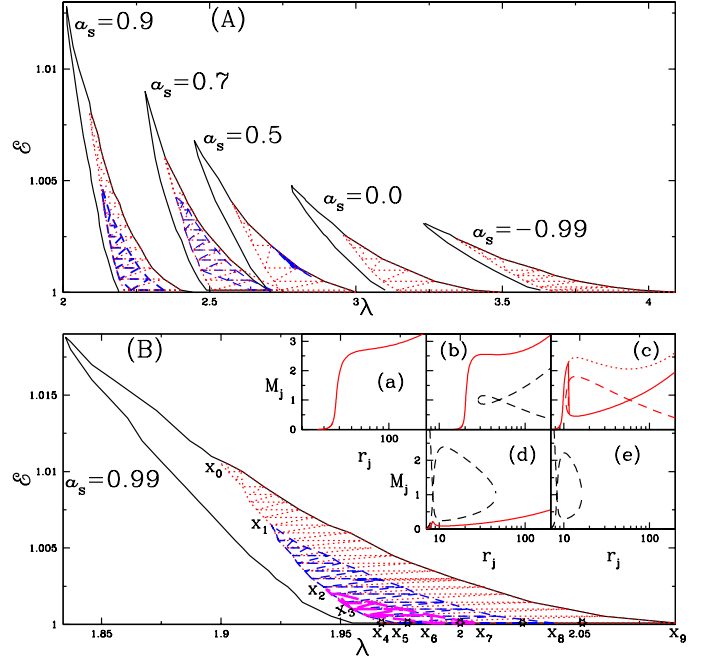


Figure 13. (A) Comparing \mathcal{E} – λ accretion shock parameter space for $a_s = -0.99, 0.0, 0.5, 0.7$ and 0.9 . (B) $a_s = 0.99$: \mathcal{E} – λ (solid black) space for accretion shock. Region $x_0x_4x_9x_0$ (dotted, red curve) represents accretion shock when mass-loss is computed. The region $x_1x_4x_8x_1$ represents \mathcal{E} – λ for which jet possesses multiple (two or three) critical points. The region $x_1x_5x_8x_1$ (dashed, blue curve) represents the accretion \mathcal{E} , λ for which the jet has three critical points. The region $x_2x_6x_7x_2$ (long-dashed, magenta curve) represents \mathcal{E} , λ for which jet harbours shock. Inset: jet Mach number (M_j) with r_j for different (a) $\lambda = 2.05$ from region $x_0x_1x_8x_9x_0$; (b) $\lambda = 2.025$ from $x_1x_5x_8x_1$; (c) $\lambda = 2.0$ from $x_2x_6x_7x_2$, (d) $\lambda = 1.98$ from $x_3x_5x_6x_3$ and (e) $\lambda = 1.97$ from $x_3x_4x_5x_3$. The accretion disc parameters are $\mathcal{E} = 1.0001$, $\xi = 1.0$.

we plot only the jet solution of the disc–jet system i.e. M_j as a function of r_j for accretion disc parameters $\mathcal{E} = 1.0001$ and $\lambda = 2.05$ (Fig. 13Ba), $\lambda = 2.025$ (Fig. 13Bb), $\lambda = 2.0$ (Fig. 13Bc), $\lambda = 1.98$ (Fig. 13Bd) and $\lambda = 1.97$ (Fig. 13Be). The disc parameters chosen for $a_s = 0.99$ are marked as stars in \mathcal{E} – λ space (Fig. 13B). The angular momentum value of x_4 is $\lambda_{x_4} = 1.967$, x_5 is $\lambda_{x_5} = 1.972$, x_6 is $\lambda_{x_6} = 1.988$, x_7 is $\lambda_{x_7} = 2.006$, x_8 is $\lambda_{x_8} = 2.039$ and x_9 is $\lambda_{x_9} = 2.09$. Each set of the disc parameters are chosen such that all possible jet solutions can be obtained. It is interesting to note that the parameter space for steady shocks shrinks, when self-consistent massloss is considered. It means that there is a possibility of shock instability that is caused by the launching of the jets. Figure (13Be) shows that the resulting jet solution is actually a closed solution. Although the accretion disc energy $\mathcal{E} > 1$ and so is the jet Bernoulli parameter

| Points in $\mathcal{E} - \lambda$ | Accretion \mathcal{E} | Accretion λ | $v_{j\infty}$ | $R_{\dot{m}}$ | Shock in jet |
|-----------------------------------|-------------------------|---------------------|---------------|---------------|--------------|
| x_0 | 1.0105 | 1.903 | 0.353 | 0.055 | NO |
| x_1 | 1.0065 | 1.921 | 0.232 | 0.059 | NO |
| x_2 | 1.002 | 1.946 | 0.146 | 0.062 | YES |
| x_3 | 1.00035 | 1.964 | Bound Jet | NA | NA |
| x_4 | 1.0001 | 1.967 | Bound Jet | NA | NA |
| x_5 | 1.0001 | 1.973 | 0.028 | 0.0774 | NO |
| x_6 | 1.0001 | 1.988 | 0.0667 | 0.0845 | YES |
| x_7 | 1.0001 | 2.006 | 0.0838 | 0.0782 | YES |
| x_8 | 1.0001 | 2.039 | 0.08196 | 0.045 | NO |
| x_9 | 1.0001 | 2.09 | 0.0384 | 0.0025 | NO |

Table 1. The coordinates of locations $x_0 - x_9$ in the $\mathcal{E} - \lambda$ parameter space of the accretion disc as in Fig.(13B) and the measure of corresponding jet properties in terms of $v_{j\infty}$ and $R_{\dot{m}}$.

\mathcal{E}_j (see equation 26), the effective Bernoulli parameter for the jet $\mathcal{B}_j < 1$. Therefore, there is no global jet solution, for this \mathcal{E} and λ . In other words, we predict from theoretical considerations that even if there is an accretion shock, the PSD may not always launch a jet. It may be noted that in Figs (12c) and (f), the jet terminal speed obtained for low to moderate disc energies decreases with the increase of a_s . However, from Figs (13 A) and (B), we observe that the maximum value of energy parameter (of Fig. 13) for which steady accretion shock is possible increases with a_s , which might launch jets with higher terminal speeds. The various coordinates e.g. $x_0 - x_9$ in $\mathcal{E} - \lambda$ accretion shock parameter space of Fig. (13B) and corresponding jet properties are tabulated in Table 1.

Fig. 14(a) represents variation of jet shock location r_{jsh} with the disc angular momentum λ , around two BHs of spin $a_s = 0.99$ (solid, red) and $a_s = 0.9$ (dotted, blue). Corresponding jet compression ratio R_j (Fig. 14b) and jet strength \mathcal{J}_s (Fig. 14c) are plotted as a function of r_{jsh} . The jet shock r_{jsh} is formed closer to the BH, if the spin parameter is higher. However, the most interesting aspect is that the jet shock becomes stronger as r_{jsh} shifts to larger values for a BH of same spin. Infact, the compression ratio for $a_s = 0.99$ is quite high, and therefore should be a good site for particle acceleration. This nature of jet shock is completely op-

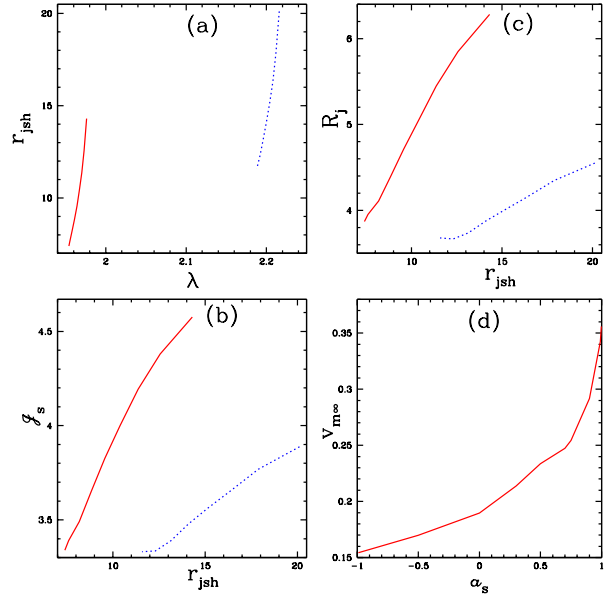


Figure 14. Variation of (a) jet shock location (r_{jsh}) with λ , (b) jet shock compression ratio R_j and (c) jet shock strength \mathcal{J}_s with r_{jsh} , where each curve is for $a_s = 0.99$ (solid, red), 0.9 (dotted, blue) and all the plots are for $\mathcal{E} = 1.001$. (d) Maximum jet terminal velocity ($v_{m\infty}$) with a_s .

posite of accretion shocks, where the accretion shock gets stronger as it is located closer to the BH (e.g. Fig. 11b). In Fig.(14d), maximum possible jet terminal speed $v_{m\infty}$ is plotted as a function of a_s . Maximum jet terminal around a BH of $a_s = 0.99$ is possible, if the jet originates from a disc that corresponds to the parameters of x_0 point of the $\mathcal{E} - \lambda$ space of Fig. (13B). Therefore, for BH of any spin, the jet corresponding to its respective x_0 point will produce a jet with maximum possible terminal speed for a BH of that particular spin. Fig. (14d) is obtained by finding the $v_{m\infty}$ for BHs of each a_s . Therefore, BH spin automatically does not produce very high speed jet, but the maximum terminal speed of a jet definitely increases with increasing BH spin.

5 DISCUSSIONS AND SUMMARY

We have studied accretion–ejection solutions in full general relativistic prescription, where the fluid is described by variable adiabatic index (Γ) EoS around Kerr BHs. The mass outflow rate from accretion disc has been estimated self-consistently by solving accretion equations of motion along the equatorial plane and jet solutions along VZS.

The accretion solution has two major improvements

over some of the previous studies. We consider a variable Γ EoS for electron–proton fluid. However, we have not considered heating or cooling processes in our analysis of the disc, because our main focus is to obtain jets self-consistently from the disc and how the BH spin affects the jets. Suffice is to say that we have in numerous previous occasions studied dissipative accretion discs around non-rotating BHs (Chattopadhyay & Das 2007; Lee *et al.* 2011; Kumar & Chattopadhyay 2013, 2014; Kumar *et al.* 2014; Chattopadhyay & Kumar 2016; Lee *et al.* 2016), and based on our accumulated knowledge, we are confident that the results presented here will qualitatively remain the same, although quantitative changes are not ruled out. While discussing Figs. (3a-e), some of the solutions (dotted) related to the accretion solutions were termed wind type. However, these solutions are not actual wind or outflow solution, since winds and jets flow in the off-equatorial direction, while the so-called wind solutions of Figs. (3a-e) are along the equatorial plane.

One of the reasons to consider accretion discs and jets in full general relativity is that relativistic formulation of jets is generally faster than the Newtonian versions, since the coupling between gravity and thermal terms (middle term of \mathcal{N}_j in equation 29) is missing in the latter. If one compares equation (29) with the equation of motion of radial or conical outflow in Schwarzschild metric, then it is easy to identify significance of each of the three terms of \mathcal{N}_j (see discussion related to equation 29). The comparison also shows that the first two terms of \mathcal{N}_j for conical flow are positive definite and only the third of the gravity term is negative. Therefore only one sonic point is possible in conical flow in Schwarzschild metric. This is also mostly true for rotating matter flowing out along the VZS around BHs of low spin. However, for higher spin parameter, the metric component along the VZS changes sign from being highly negative to positive. This causes the jet to become transonic very close to the BH. And because the same term flips sign along the VZS, this may decelerate the supersonic flow and may cause the formation of multiple sonic points and shocks in jets.

The jet streamline and cross-section are a major issue in analytical studies of accretion-jet system. It has been shown

earlier that VZS are the surfaces of constant angular momentum and also of constant entropy for fluid flow above the equatorial plane (Chakrabarti 1985). In addition, numerical simulations showed that the entire PSD generates bipolar jets (Molteni *et al.* 1996b; Lanzafame *et al.* 1998; Das *et al.* 2014; Lee *et al.* 2016). So, we choose the foot point (r_b) of the jet streamline located half way between the accretion shock and inner critical point of the disc, but on the surface of PSD. Once we obtain the base of the streamline or r_b , we solve for VZS from the disc properties at (r_b, θ_b) on PSD surface. Therefore, the VZS is the streamline, and the cross-sectional area between r_{ci} and r_{sh} orthogonal to the VZS is the jet cross-sectional area. This simplifies the jet structure and make the problem tractable analytically. With these considerations, the jet streamline and the associated cross-section depend on the disc parameters like \mathcal{E} and λ , as well as on the spin of the BH, which is a major improvement on the jet geometry assumed in the pseudo-Newtonian regime (Chattopadhyay & Das 2007; Kumar & Chattopadhyay 2013; Aktar *et al.* 2015). Moreover, the jet solution from the disc is launched with very low velocity along the streamline, but becomes supersonic at a short distance from the base of the jet. This is because the metric term h_p along the VZS for highly spinning BH powers the jet. This entire analysis was at first implemented by us in our previous paper for Schwarzschild geometry (Chattopadhyay & Kumar 2016); now we have upgraded it to the Kerr metric.

The jet generated depends on the compression ratio (R) of the accretion shock, the upward thrust of the PSD and the ratio between jet cross-section with the surface of the PSD. So the mass outflow rate can be shown to increase with the increasing R ; however, within few r_g of the BH, the upward thrust and/or the fractional jet cross-section may reduce, making the mass outflow rate to dip. The relative mass outflow rate for given disc energy parameters also increases with the spin of the BH. However, the angular momentum range of the accretion discs to obtain such jets moves to the lower values if the BH spin parameter is increased. The dependence of the terminal speed of the jet with BH spin is not straightforward, since the jet is gen-

erated by the accretion disc. And accretion disc properties depend as much on the properties of the central BH as on the boundary conditions of the disc itself. So if the accretion disc parameters are of moderate values, the jet produced will be weak, no matter what the value of BH spin parameter is. However, the maximum jet speed for steady jets increases with the spin of the BH. The maximum jet speed obtained in this paper for $a_s = 0.99$ is about $v_{j\infty} \sim 0.35$, which is not truly relativistic. It is to be remembered that jets from around compact objects like BHs are not always ultrarelativistic. Not only the terminal speed of jets varies in various objects, even for the same object the jet varies in strength in different epochs (Miller-Jones *et al.* 2012). Having said that, in this paper we were interested to find out the effect of BH spin on jet formation and therefore no additional accelerating process for the jet was considered. Thermally driven jets are unlikely to generate relativistic terminal speed. Previous studies of accretion-jet system in the pseudo-Newtonian regime could generate jets of terminal speed $\sim \text{few} \times 0.01$ (Chattopadhyay & Das 2007; Kumar & Chattopadhyay 2013). However, if these jets are accelerated by radiation from the disc then the terminal speed achieved is ~ 0.3 (Kumar *et al.* 2014)! Even if there is no radiation driving, then shock oscillation can power jets to around $\sim \text{few} \times 0.1$ (Lee *et al.* 2016). In the present paper, consideration of relativistic equations of motion in Kerr metric, relativistic EoS and obtaining the VZS from the accretion disc, all have contributed in obtaining terminal speeds that are atleast an order of magnitude faster (compared to jets in pseudo-Newtonian regime), even for thermally driven jets. Moreover, in this paper we have only studied the electron–proton jets, which are heavier. A finite proportion of electron–positron pair might be conducive for radiative or magnetic acceleration to much higher terminal speeds. Infact, radiation momentum deposition from luminous discs onto a jet composed of protons, electrons and positrons can very well accelerate jets to terminal speeds in excess of 90 percent of light speed (e. g., fig. 11 of Vyas *et al.* 2015). Therefore, investigation of radiative acceleration of self-consistent jets from accretion discs around Kerr BHs, in

the footsteps of Kumar *et al.* (2014), should yield encouraging results.

In this paper, we studied the jet solutions ejected from the accretion disc. In all our previous studies of accretion-jet system around a non-rotating BH, we found only monotonic jet solution. In this paper, we find all possible solutions for jets too. Therefore, not only we have strong jets that become transonic very close to the BH or shocked jets or weak jets that become transonic at large distances, but also bound jet solutions. That means there may be accretion shocks but there may not be jet if the accretion disc parameters fall in a particular part of the parameter space. The bound jet solutions may qualify as failed jets. In this paper, we have mapped various jet solutions in terms of the accretion disc parameters, which will give an idea about which range of disc parameters will generate jets and which will not.

The shock in jet is rather strong > 4 , especially around highly spinning BH. While the accretion shock becomes stronger as it shifts closer to the BH, the shock in jet becomes stronger as it moves outwards. And jet begins to harbour shocks at $a_s > 0.6$. So detection of strong jet shocks close to the BH and in the jet might indicate that the BH is spinning. Moreover, the presence of shock in the jet as well as in the accretion disc would produce hot flow around the equatorial plane and also close to the poles too. Since the accretion and jet shock are obtained very close to the horizon, therefore if radiation hydrodynamics of such shocks indeed produce soft gamma-ray tail, then it may vindicate Laurent *et al.* (2011).

One may also remember that there are few studies of particle acceleration in accretion disc shocks (Le & Becker 2007; Lee & Becker 2017). With the presence of strong shocks both in accretion ($R \gtrsim 3$) and jets ($R_j \gtrsim 4$), it would be worthwhile to study particle acceleration in such accretion–ejection system, especially around highly spinning BH.

ACKNOWLEDGMENT

The authors acknowledge the anonymous referee for helpful suggestions.

REFERENCES

- Abramowicz M. A., 1971, *Acta Astr.*, 21, 81
- Aktar R., Das S., Nandi A., 2015, *MNRAS*, 453, 3414
- Artemova I. V., Bjoernsson G., Novikov I. D., 1996, *ApJ*, 461, 565
- Becker P. A., Das S., Le T., 2008, *ApJ*, 677, L93
- Blandford R. D., Payne D. G., 1982, *MNRAS*, 199, 883
- Blandford R. D., Znajek R. L., 1977, *MNRAS*, 179, 433
- Camezind M., 1986, *A&A*, 162, 32
- Chakrabarti S. K., 1985, *ApJ*, 288, 7
- Chakrabarti S.K., 1989, *ApJ*, 347, 365
- Chakrabarti S. K., Titarchuk L., 1995, *ApJ*, 455, 623
- Chakrabarti S.K., 1996, *MNRAS*, 283, 325
- Chakrabarti S. K., Mondal S., 2006, *MNRAS*, 369, 976
- Chandrasekhar S., 1939, *An Introduction to the Study of Stellar Structure*. Univ. Chicago Press, Chicago, IL
- Chattopadhyay I., Das S., 2007, *New Astron.*, 12, 454
- Chattopadhyay I., 2008, in Chakrabarti S. K., Majumdar A. S., eds, *AIP Conf. Ser. Vol. 1053, Proc. 2nd Kolkata Conf. on Observational Evidence of Black Holes in the Universe and the Satellite Meeting on Black Holes Neutron Stars and Gamma-Ray Bursts*. Am. Inst. Phys., New York, p. 353
- Chattopadhyay I., Ryu D., 2009, *ApJ*, 694, 492
- Chattopadhyay I., Chakrabarti S.K., 2011, *Int. J. Mod. Phys. D*, 20, 1597
- Chattopadhyay I., Kumar R., 2013, in Das S., Nandi A., Chattopadhyay I., eds, *Astronomical Society of India Conference Series*, Vol. 8, p. 19
- Chattopadhyay I., Kumar R., 2016, *MNRAS*, 459, 3792.
- Cox J. P., Giuli R. T., 1968, *Principles of Stellar Structure*, Vol.2: Applications to Stars. Gordon and Breach, New York
- Das S., Chattopadhyay I., Nandi A., Molteni D., 2014, *MNRAS*, 442, 251.
- Doeleman S. S. et al., 2012, *Science*, 338, 355.
- Fender R. P., Belloni T. M., Gallo E., 2004, *MNRAS*, 355, 1105
- Fender R. P., Gallo E., Russell D., 2010, *MNRAS*, 406, 1425
- Fendt C., Greiner J., 2001, *A&A*, 369, 308
- Ferrari, A., 1998, *ARA&A*, 36, 539
- Fukue J., 1987, *PASJ*, 39, 309
- Fukumura K., Tsuruta S., 2004, *ApJ*, 611, 964
- Fukumura K., Kazanas D., 2007, *ApJ*, 669, 85
- Gallo E., Fender R. P., Pooley G. G., 2003, *MNRAS*, 344, 60
- Giri K., Chakrabarti S. K., 2013, *MNRAS*, 430, 2826
- Junor W., Biretta J. A., Livio M., 1999, *Nature*, 401, 891
- Kozłowski M., Jaroszynski M., Abramowicz M. A., 1978, *A&A*, 63, 209
- Kumar R., Chattopadhyay I., 2013, *MNRAS*, 430, 386
- Kumar R., Chattopadhyay I., 2014, *MNRAS*, 443, 3444
- Kumar R., Singh C. B., Chattopadhyay I., Chakrabarti S. K., 2013, *MNRAS*, 436, 2864
- Kumar R., Chattopadhyay I., Mandal S., 2014, *MNRAS*, 437, 2992
- Lanzafame G., Molteni D., Chakrabarti S. K., 1998, *MNRAS*, 299, 799
- Laurent P., et. al., 2011, *Science*, 332, 438.
- Le T., Becker P. A., 2007, *ApJ*, 661, 416
- Lee S.-J., Ryu D., Chattopadhyay I., 2011, *ApJ*, 728, 142
- Lee S.-J., Chattopadhyay I., Kumar R., Hyung S., Ryu D., 2016, *ApJ*, 831, 33.
- Lee J. P., Becker P. A., 2017, *MNRAS*, 465, 1409
- Liang E. P. T., Thompson K. A., 1980, *ApJ*, 240, 271
- Lu J. F., 1985, *A&A*, 148, 176
- Lu J. F., Gu W. M., Yuan F., 1999, *ApJ*, 523, 340
- Marscher, A. P., et. al., 2002, *Nature*, 417, 625
- McHardy I. M., Koerding E., Knigge C., Fender R. P., 2006, *Nature*, 444, 730
- Miller-Jones J. C. A., Sivakoff G. R., Altamirano D., et al., 2012, *MNRAS*, 421, 468
- Mirabel, I. F., et. al., 1992, *Nature*, 358, 215
- Mirabel, I. F., Rodriguez, L. F., 1994, *Nature*, 371, 46
- Molteni D., Lanzafame G., Chakrabarti S. K., 1994, *ApJ*, 425, 161
- Molteni D., Sponholz H., Chakrabarti S. K., 1996a, *ApJ*, 457, 805
- Molteni D., Ryu D., Chakrabarti S. K., 1996b, *ApJ*, 470, 460
- Mukhopadhyay B., 2003, *ApJ*, 586, 1268
- Nagakura, H., Yamada, S., 2008, *ApJ*, 689, 391
- Nakayama, K., 1994, *MNRAS*, 270, 871
- Nakayama, K., 1996, *MNRAS*, 281, 226
- Narayan R., McClintock J. E., 2012, *MNRAS*, 419L, 69
- Narayan R., Yi I., 1994, *ApJ*, 428, L13
- Narayan R., Kato S., Honma F., 1997, *ApJ*, 476, 49
- Novikov I. D.; Thorne K. S., 1973, in Dewitt B. S., Dewitt C., eds, *Black Holes*. Gordon and Breach, New York, p. 343
- Paczyński B., Wiita P. J., 1980, *A&A*, 88, 23.
- Peitz J., Appl S., 1997, *MNRAS*, 286, 681
- Penrose P., 1969, *Riv. Nuovo Cimento*, 1, 257
- Riffert H., Herold H., 1995, *ApJ*, 450, 508
- Rushton, A., Spencer, R., Fender, R., Pooley, G., 2010, *A&A*, 524, 29
- Russel D. M., Gallo E., Fender R. P., 2013, *MNRAS*, 431, 405

- Ryu D., Chattopadhyay I., Choi E., 2006, ApJS, 166, 410
 Shakura N. I., Sunyaev R. A., 1973, A&A, 24, 337S.
 Sunyaev R. A.; Titarchuk L. G.; 1980, A&A, 86, 121
 Synge J. L., 1957, The Relativistic Gas, North-Holland Publishing
 Co., Amsterdam
 Taub A. H., 1948, Phys. Rev., 74, 328
 Vyas M. K., Kumar R., Mandal S., Chattopadhyay I., 2015, MN-
 RAS, 453, 2992

APPENDIX A: CALCULATION OF h_p^2

The tangent on jet streamline at any point can be expressed as

$$x_p = mr_j \sin \theta_j + c_i, \quad (\text{A1})$$

where $m = (1 - r_j \tan \theta_j \theta_j') / (\tan \theta_j + r_j \theta_j')$ and c_i are the slope and intercept, respectively. We calculate $\theta_j = \sin^{-1} \left(\left[-s - \sqrt{s^2 - 4Z_\phi^2 a_s^2} \right] / 2a_s^2 \right)^{1/2}$ and $\theta_j' = d\theta_j/dr_j = [s' \tan \theta_j / 2] / \sqrt{s^2 - 4Z_\phi^2 a_s^2}$, from equation (23). We define $s = -[a_s^2 \lambda_j Z_\phi^2 - 2a_s r_j Z_\phi^2 + \lambda_j (r_j^2 + a_s^2)^2 - 2\lambda_j^2 a_s r_j] / (\Delta_j \lambda_j)$ and $s' = ds/dr_j = [-\lambda_j s \Delta_j' + 2a_s (Z_\phi^2 + \lambda_j^2) - 4\lambda_j r_j (r_j^2 + a_s^2)] / (\Delta_j \lambda_j)$. The basis vector along streamline is defined as

$$\mathbf{e}_p = \left(\frac{\partial r_j}{\partial x_p} \right) \mathbf{e}_r + \left(\frac{\partial \theta_j}{\partial x_p} \right) \mathbf{e}_\theta, \quad (\text{A2})$$

where $\mathbf{e}_p = h_p \hat{e}_p$, $\mathbf{e}_r = h_r \hat{e}_r$ and $\mathbf{e}_\theta = h_\theta \hat{e}_\theta$. Here, \hat{e}_p , \hat{e}_r and \hat{e}_θ are unit basis vectors along the tangent, radial and polar direction at a point, respectively. The magnitude of the basis vector is written as

$$h_p^2 = h_r^2 \left(\frac{\partial r_j}{\partial x_p} \right)^2 + h_\theta^2 \left(\frac{\partial \theta_j}{\partial x_p} \right)^2, \quad (\text{A3})$$

where $h_r^2 = g_{rr} = \Sigma_j / \Delta_j$ and $h_\theta^2 = g_{\theta\theta} = \Sigma_j$ are Kerr metric components. For the calculation of h_p , we have taken partial differentiation of equations (23) and (A1) with respect to x_p ; we get

$$K^2 \left(\frac{\partial r_j}{\partial x_p} \right)^2 = \cot^2 \theta_j \left(\frac{\partial \theta_j}{\partial x_p} \right)^2$$

$$\text{and } \cos^2 \theta_j = C_r^2 \left(\frac{\partial r_j}{\partial x_p} \right)^2 + C_\theta^2 \left(\frac{\partial \theta_j}{\partial x_p} \right)^2, \quad (\text{A4})$$

where $C_r = [\cos^2 \theta_j - r_j^2 K' - r_j K (2 + r_j K) \sin^2 \theta_j] / (1 + r_j K)^2$, $C_\theta = r_j \tan \theta_j [\cos^2 \theta_j + r_j K / (1 + r_j K)]$, $K = s' / 2(s^2 - 4a_{r_s}^2 Z_\phi^2)^{1/2}$, $K' = dK/dr_j = K(s'' - 4sK^2) / s'$ and $s'' = -2[s + s' \Delta_j' + 2(3r_j^2 + a_{r_s}^2)] / \Delta_j$. Using equation (A4) in equation (A3), then we get the expression of h_p ,

$$h_p^2 = \frac{\cos^2 \theta_j [h_r^2 + h_\theta^2 K^2 \tan^2 \theta_j]}{[C_r^2 + C_\theta^2 K^2 \tan^2 \theta_j]} \quad (\text{A5})$$